5-24-2012

Interactions of Cardiomyocytes and Myofibroblasts: An Experimental and Theoretical Model Study

Teresa Abney
Washington University in St. Louis

Recommended Citation

Abney, Teresa, "Interactions of Cardiomyocytes and Myofibroblasts: An Experimental and Theoretical Model Study" (2012). *All Theses and Dissertations (ETDs)*. 677.
https://openscholarship.wustl.edu/etd/677

WASHINGTON UNIVERSITY IN ST. LOUIS

School of Engineering and Applied Science

Department of Mechanical Engineering and Materials Science

Thesis Examination Committee:
Guy Genin, Chair
Philip Bayly
Igor Efimov
Elliot Elson
Ruth Okamoto
Yoram Rudy
Larry Taber

Interactions of Cardiomyocytes and Myofibroblasts:

An Experimental and Theoretical Model Study

by

Teresa M. Abney

A dissertation presented to The Graduate School of Arts & Sciences
of Washington University in partial fulfillment of the
requirements for the degree of

DOCTOR OF PHILOSOPHY

May 2012
Saint Louis, Missouri

ABSTRACT OF THE THESIS

Interactions of Cardiomyocytes and Myofibroblasts:
An Experimental and Theoretical Model Study
by
Teresa M. Abney
Doctor of Philosophy in Mechanical Engineering
Washington University in St. Louis, 2012
Research Advisor: Professor Guy Genin

Cardiomyocytes and fibroblasts make up the majority of cells in natural myocardium. While cardiomyocytes are primarily responsible for the mechanical contraction, fibroblasts are responsible for maintaining the extracellular matrix and tissue compliance. In response to pathologies such as hypertension or infarction, fibroblasts in the heart can convert to myofibroblasts, a larger and more contractile phenotype between a fibroblast and a smooth muscle cell. Myofibroblasts are essential to wound healing, but can change the compliance and functioning of heart tissue and can produce pathological fibrosis, formation of excess fibrous connective tissue. In developing therapeutic approaches it is essential to understand how myofibroblasts modulate the electromechanical functions of fibrotic heart. In this dissertation, the problem was approached by developing computational and experimental models of heart muscle with varying proportions of mFBs to CMs randomly distributed. The experimental model consists of engineered heart tissue (EHT) assembled from embryonic cardiomyocytes and containing defined fractions of myofibroblasts randomly distributed throughout the tissue. The computational model is formulated at the cellular level taking into account individual cardiomyocytes and myofibroblasts to yield the pattern of impulse spread as modulated by the presence of myofibroblasts acting either as insulators or resistors. The excitatory impulse activates the contraction of individual viscoelastic cells that are mechanically linked to other cells and the extracellular matrix. The results give insight into the mechanical and electrical modulation of EHT by myofibroblasts.

Acknowledgments

I would like to acknowledge my research advisors, Dr. Guy Genin and Dr. Elliot Elson. Thank you for your support and inspiration. I am grateful also to everyone in the Elson/Genin lab for their contributions to this work. Specifically, I would like to thank Tony Pryse for his patience in guiding me through the challenging world of biological experiments.

Finally, I am grateful for the financial support in part by the NIH (K25 HL079165 and R01 GM069072) and also by the NSF through a graduate research fellowship (DGE-1143954).

Teresa M. Abney

Washington University in Saint Louis
May 2012

I would like to dedicate this dissertation to my wonderful family.

To my parents, Chris and Chuck Abney, who have always supported me in my academic and career pursuits, and have instilled upon me the importance of hard work and diligence. To my big brother, Captain Charles Abney, who has been an amazing role model of leadership and strength. Finally, to my extremely understanding husband-to-be, Matt Spencer, who has supported and encouraged me in every step of my research.

Contents

List of Figures

Chapter 1

Introduction

Cardiomyocytes and fibroblasts make up the majority of cell types in the natural myocardium [41]. While cardiomyocytes are primarily responsible for the mechanical contraction, fibroblasts are responsible for maintaining the extracellular matrix and tissue compliance. Under certain pathological conditions though, such as hypertension or infarction, this delicate balance can be disrupted [27]. In response to such an injury, normal fibroblasts convert to myofibroblasts (mFBs), a larger and more contractile phenotype intermediate between a fibroblast and a smooth muscle cell.

In contrast to the normal fibroblast, the mFBs expresses α-smooth muscle actin (α-SMA), which is essential to its increased contractility, but, unlike a smooth muscle cell, it retains its capacity for secreting collagen. Both contractile and collagen synthetic capabilities are necessary for wound healing. Nevertheless, mFBs can produce a pathological condition, fibrosis (the formation of excess fibrous connective tissue), in a variety of organs, e.g., lung, kidney, liver, and heart. When cardiomyocytes (CMs) in a defined region of the heart muscle die due to a blockage of the blood supply (myocardial infarction), the formation of an infarct scar produced and maintained by mFBs stabilizes the damaged portion of the muscle. Although this response preserves the overall function of the heart, the infarct scar both presents a mechanical mismatch to the undamaged heart muscle, impairing heart contraction, and can serve as a focus for reentrant arrhythmias, potentially leading to sudden death. (A reentrant arrhythmia occurs when depolarization spreads through a region of the heart and then returns abnormally to depolarize its site of initiation.) Conversely, hypertension produces a quasi-random interstitial distribution of mFBs that can lead to reentrant arrhythmias and also stiffens the left ventricle, reducing its ability to relax and therefore its ability to fill during diastole (diastolic dysfunction, [13]).

The ability to control the damaging effects of mFBs in the heart would be a great public health benefit. It is not clear, however, that simply preventing the formation of mFBs or abolishing their effects in the heart would be suitable since some level of mFB function is adaptive in myocardial infarction and possibly also in hypertension. In developing therapeutic approaches it is therefore essential to understand how mFBs interact with CMs to modulate the electromechanical functions of the heart, and how changes in mFB function, e.g., attenuation of mFB contractility or partial elimination of interstitial mFBs, would affect these functions.

In this dissertation, the problem was approached by developing computational and experimental models of heart muscle with varying proportions of mFBs to CMs randomly distributed. The computational model is formulated at the cellular level taking into account individual CMs and mFBs to yield the pattern of impulse spread as modulated by the presence of mFBs acting either as insulators or resistors. The excitatory impulse activates the contraction of individual viscoelastic cells that are mechanically linked to other cells and the extracellular matrix (ECM). The experimental model consists of engineered heart tissues (EHTs) assembled from embryonic CMs and containing defined fractions of mFBs randomly distributed throughout the tissue. Validation of the former by comparison to experimental measurements of EHT assembled to reveal the effects of mFBs and yield insight into the interactions of CMs and mFBs in EHT.

Initial experimental results indicated, in moderate concentrations, mFBs improved contractile EHT functioning, but at higher concentrations could impair function. In Chapter 2, this was first studied through a one-dimensional simplified mechanical model of a string of mFBs and CMs in varying ratios. The model supported the experimental results and yielded insight into possible mechanical causes for deleterious effects of mFBs on EHT. To summarize, there exists a tradeoff with the increase of mFB cell concentration. As the concentration of mFBs increases, the stiffness of the tissue increases, and this enhances the twitch transmission, but this increase also dilutes the concentration of CMs, the twitch producing cells. In addition to the mechanical effects though, myofibroblasts can impair EHT contractile function by distorting excitatory conduction, as was the focus of Chapter 3. Electrophysiologic bounds and estimates for conduction velocity in simulations of idealized fibrotic myocardium showed decreased conduction velocity with increased mFB volume fraction, and ultimately failed conduction at a critical mFB volume fraction. Expanding on these simulations in Chapter 4, experimental techniques for estimation of conduction velocity using calcium imaging compared to estimates of measured mFB volume fraction in EHT yielded further insight into the electrical effects of mFBs on EHT. Preliminary results support electrophysiologic simulations with conduction velocity decreasing with increased mFB volume fraction. Finally, Chapter 5 addresses the trade-off between electrical and mechanical percolation effects in two-dimensions. Results show that, in moderate concentrations, mFBs have little effect on overall tissue function, but at a critical mFB volume fraction, twitch force begins to decrease, and then at a critical electrical percolation threshold, conduction is completely blocked and EHT no longer contracts.

Chapter 2

Beneficial and deleterious mechanical interactions between myofibroblasts and cardiomyocytes in a one-dimensional tissue model

2.1 Introduction

When cardiomyocytes in a defined region of heart muscle die due to a blockage of the blood supply (myocardial infarction), the formation of an infarct scar, produced and maintained by myofibroblasts, stabilizes the injured portion of the muscle. Although this response preserves the overall function of the heart, the infarct scar both presents a mechanical mismatch to the native heart muscle, impairing heart contraction [17], and can serve as a focus for reentrant arrhythmias, potentially leading to sudden death. Conversely, hypertension produces a quasi-random interstitial distribution of myofibroblasts that can lead to reentrant arrhythmias and also stiffens the left ventricle, reducing its ability to relax and therefore its ability to fill during diastole (diastolic dysfunction, [13].)

The ability to control the damaging effects of myofibroblasts in the heart would evidently be a great public health benefit. It is not clear, however, that simply preventing the formation of myofibroblasts or abolishing their effects in the heart would be suitable since some level of myofibroblast function is adaptive in myocardial infarction and possibly also in hypertension. In developing therapeutic approaches it is therefore essential to understand how myofibroblasts interact with cardiomyocytes to modulate the electromechanical functions of the heart, and how changes in myofibroblast function, e.g., attenuation of myofibroblast contractility or partial elimination of interstitial myofibroblasts, would affect these functions.

This problem was studied through computational and experimental models of heart muscle with defined fractions of myofibroblasts. The experimental model consists of engineered heart tissue (EHT) assembled from embryonic cardiomyocytes and containing defined fractions of myofibroblasts randomly distributed. EHT has been shown to replicate many features of the biophysics of natural myocardium [42, 7, 3]. Data from our experimental model suggested that a range of concentrations of myofibroblasts promote periodic contraction of EHT, while higher concentrations obstruct this.

Based upon these data it was hypothesized that myofibroblasts initially serve an adaptive mechanical role by enhancing contractile function of EHT in moderate concentrations, although they can impair EHT function at high concentrations. While a potential role of conduction disruption in fibrotic effects on heart tissue has long been explored, the mechanical role of myofibroblasts and the mechanical consequences of fibrotic remodeling have not. A mathematical model was developed to delineate how mechanical effects of myofibroblasts can explain our experimental observations. The mathematical model was formulated at the cellular level with individual viscoelastic cells linked mechanically to other cells and the extracellular matrix (ECM). Parametric studies isolating the effects of myofibroblast overgrowth and the associated changes to the extracellular matrix yielded insight into how myofibroblasts alter tissue mechanics, and suggested a mechanical mechanism for the observed beneficial and deleterious effects of myofibroblasts on EHT contraction. We observed that stiffening of an EHT by myofibroblasts improved twitch force transmission, that dilution of the concentration of cardiomyocytes in an EHT by overgrowth of myofibroblasts impaired twitch force, and that the trade-off between the two led to optimum contractility.

2.2 Methods

2.2.1 Experimental methods

EHT specimens were prepared as described previously [7] by isolating cardiomyocytes from 10-day-old chicken embryos, and suspending the cells (approximately 1.4 million/ml, final concentration) in Type I rat tail collagen, DMEM with 10% FBS, and 4% chicken embryo extract. The mixture was poured into a mold and placed in a 37°C CO_2 incubator producing a loose collagen gel in which cells are randomly distributed. Within 5-7 days the cardiomyocytes began contracting independently and the EHT twitch force was readily measurable with an isometric force transducer. EHT specimens were mounted onto a tensile testing device with stepper motor and an integrated isometric force transducer system described previously [34]. This device was used to obtain mechanical measurements of twitch and baseline force.

Experiments to identify effects of myofibroblasts on EHT contraction were conducted in two ways. First, EHT specimens were made with prescribed concentrations of myofibroblasts, and twitch and baseline forces were monitored as a function of time as myofibroblasts proliferated but cardiomyocytes did not.

Second, other EHT specimens were treated with cytochalasin D, an inhibitor of the actin cytoskeleton in myofibroblasts, and observed over time while the mechanical effects of myofibroblasts decreased. In these experiments, EHT specimens were mounted in an organ bath with HEPES-buffered DMEM at 37°C, and F-actin was disrupted using 0.05 μM cytochalasin D (Sigma, St. Louis, MO) to gradually reduce contributions of myofibroblasts to EHT specimen's mechanics. While this did not eliminate entirely the increased stiffness of the ECM by myofibroblasts (e.g. [19, 18]), the disruption of the myofibroblast actin cytoskeletons did decrease the stiffness of the extracellular mechanical environment of the cardiomyocytes. The stiffness and the contractile force exerted by myofibroblasts have been shown to be directly proportional to the degree of actin stress fiber polymerization [23], and the degree of disruption of the actin cytoskeleton increases with the concentration of cytochalasin D [35]. The rationale for this second protocol is that our simulations showed stiffening of the extracellular environment to be a central factor in determining the degree to which cardiomyocyte contraction translated to tissue level contraction, and this graded reduction in myofibroblast stiffness reduced extracellular stiffness in a controlled way.

Relating experiments to predictions involved converting volume fractions of cardiomyocytes and myofibroblasts to the ratio of myofibroblasts to the total number of cells (Θ). Experimental force data, normalized to start at one, were correlated to computational estimates as a function of Θ. The mechanics of the extracellular environment was also a function of Θ. In analogous tissue constructs containing only one cell type, myofibroblasts, the baseline force (constant minimum contractile force exerted by the system) has been shown proportional to the total amount of un-disrupted F-actin in all cells in the tissue construct [23]. We extrapolated this observation to motivate a linear relationship between baseline force and Θ. The range of Θ was calculated from myofibroblast and cardiomyocyte area fractions of EHT, as published by [3], by approximating a cardiomyocyte to be 5 times the volume of a myofibroblast [39, 38]. In experiments involving deoxycholate treatment, $\Theta=0$ corresponded to the condition in which all myofibroblasts were affected, and intermediate values of Θ were extrapolated between 0 and the pre-treatment value.

2.2.2 Mathematical models of cells and tissue

The computational goal of this work was to predict the mechanical effects of myofibroblasts on the mechanical functioning of EHT specimens. The model comprised several existing models of cells within an ECM.

Cardiomyocytes

CMs were modeled in one dimension as modified Hill elements with an active, dynamic element that produced a dynamic force $\bar{F}(t)$, a passive parallel element of stiffness k^p, a series stiffness k^s, and a viscosity c^p (Figure 2.1) [12, 36] . The parallel stiffness represented the inherent compliance of the contractile assembly of a cell. The series stiffness represented compliance such as that associated with titin that transmits forces to the ends of the specimen [36]. Although our earlier work showed that cells of many types exhibit nonlinear elasticity [40, 34], we applied this linear viscoelastic model of passive cell mechanics as a first order approximation that is valid strictly only in the sense of incremental behavior [25].

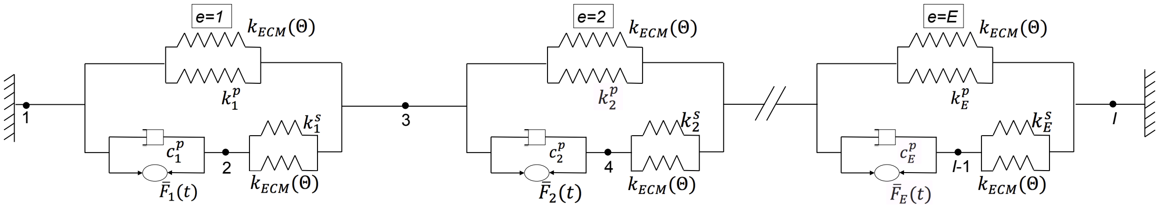

Figure 2.1: Schematic of the one-dimensional mechanics model
The one-dimensional mechanics model begins with a string of all CMs. CMs are gradually and randomly replacing with mFBs to represent the overgrowth of EHT. CMs were modeled as modified hill elements with a dynamic contractile twitch force while mFBs differed from CMs by material properties as well as the force was converted to a static contractile force.

Standard models reproduced the active tension developed through twitching of the cardiomyocytes. The twitch profile $\bar{F}(t)$ was developed from the Hunter-McCulloch-ter Keurs (HMT) model shown in Figure 2.2 [12, 24], based upon a model of the intracellular calcium concentration transient (see Appendix A). Briefly, cardiomyocyte contractile stress depends on the concentration of free myoplasmic calcium, the cellular stretch rate, and its time history. The internal workings of the model involve three state variables: the concentration of calcium bound to troponin C, the fraction of actin binding sites that are occupied by actomyosin crossbridges, and the state-dependent maximum activation stress. As appropriate for these isometric tests, no feedback between mechanical strain and twitching contraction was included.

Myofibroblasts

Myofibroblasts were modeled to first order following Zahalak [40] as modified Hill elements. These elements differed from the cardiomyocyte elements in that the dynamic twitch force was replaced by a steady, static contractile force, and their passive mechanical parameters were allowed to differ from those of the cardiomyocytes. Myofibroblasts were in parallel with ECM.

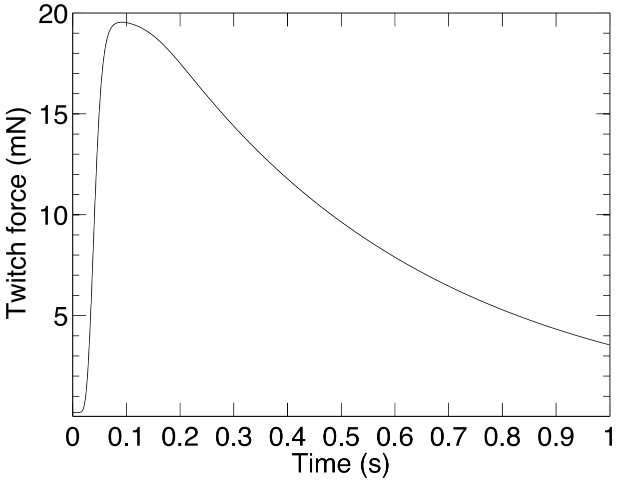

Figure 2.2: Twitch force profile for an individual CM
A twitch force profile for an individual CM, as described by the theoretical HMT model, was used for the contractile force in the mechanics model.

Extracellular matrix

ECM was modeled as linear and elastic. Following the observations of Marquez et al. [19, 18], the modulus of the extracellular matrix increased with increasing density of myofibroblasts. The increase in modulus with increasing myofibroblast concentration exceeds that expected from the reduction of cross-sectional area caused by the compression of the construct by the myofibroblasts [19]. Thus, the structural stiffness afforded by the ECM (modulus × cross-sectional area) increased as well with increasing myofibroblast density. ECM was modeled as a spring in parallel with each cell with stiffness k_{ECM}. ECM stiffness was assumed to be related to Θ by $k_{ECM} = \alpha\Theta$ where α was an unknown proportionality constant studied over a broad range of possibilities.

Tissue

Tissue was modeled in one dimension as a string of cells connected in series mechanically, each connected in parallel with ECM. In the absence of myofibroblasts, the string of cells was an uninterrupted chain of cardiomyocytes representative of a muscle fiber, with each cell in parallel with relatively compliant ECM. Tissue overgrowth by myofibroblasts was modeled by increasing the fraction of myofibroblast elements distributed randomly in the string of cells. The stiffnesses of cells and ECM were permitted to vary over a broad range.

2.2.3 Computational methods

One-dimensional strings of discrete cells were studied. A typical simulation included 100 cells. To model our isometric experiments, the ends of the model were restrained from moving, and the time-varying isometric force was predicted. The string of cells was initially entirely CMs, but varying concentrations of CMs were replaced by mFBs to explore the one-dimensional mechanical effects of mFBs on EHT.

The governing equations were solved using a combined finite element and finite difference method, with inertial terms neglected as is appropriate for the isometric conditions tested. Inertial terms were small in the reconstituted tissue systems studied, even in the cases of rapid and nonlinear contraction [23]. Thus, an incrementally quasi-static approach was adopted: at each time step, twitch forces and dynamic viscoelastic terms were calculated using a backward difference approach, and cell and ECM forces and displacements were calculated using a finite element approach.

The governing equations were developed by assigning nodes $i = 1, 2, 3, \ldots I$ between the cells (numbered $e = 1, 2, 3, \ldots E$) and within each cell between the series spring and force-producing component; the convention adopted was that odd numbered nodes separated cells, and even numbered nodes were internal to cells. Momentum balance equations were written to determine the internal force f_i at each node. Momentum balance at the end node required that:

$$f_1(t) = (k_1^p + k_{ECM}(\Theta))\,(u_1(t) - u_3(t)) + c_1^p(\dot{u}_1(t) - \dot{u}_2(t)) + \bar{F}_1(t). \tag{2.1}$$

where k_1^p is the parallel stiffness of cell e=1, $k_{ECM}(\Theta)$ is the ECM stiffness, a function of Θ, c_1^p is the viscosity of cell e=1, $u_1(t)$, $u_2(t)$, and $u_3(t)$ are the displacements of nodes i=1, 2 and 3, respectively, and $\bar{F}_1(t)$ is the contractile force of cell e=1 (dynamic twitch force for a cardiomyocyte or static contractile for a myofibroblast). $\dot{()}$ denotes a derivative with respect to time. Momentum balance within the internal node of each cell, e, required:

$$f_{i(even)} = (k_e^s + k_{ECM}(\Theta))(u_i(t) - u_{i+1}(t)) - c_e^p(\dot{u}_{i-1}(t) - \dot{u}_i(t)) - \bar{F}_e(t) \quad (2.2)$$

where $e = i/2$, k_e^s is the e^{th} cell's series stiffness, k_e^p is e^{th} cell's parallel stiffness, c_e^p is e^{th} cell's viscostiy, $u_i(t)$ is the displacement of the i^{th} node, and $\bar{F}_e(t)$ is the e^{th} cell's contractile force (again, dynamic twitch force for a cardiomyocyte or static contractile for for a myofibroblast). Momentum balance for nodes between cells required:

$$\begin{aligned} f_{i(odd)} = {} & (k_{e+1}^p + k_{ECM}(\Theta))(u_i(t) - u_{i+2}(t)) + c_{e+1}^p(\dot{u}_i(t) - \dot{u}_{i+1}(t)) + \bar{F}_{e+1}(t) \\ & - (k_e^s + k_{ECM}(\Theta))(u_{i-1}(t) - u_i(t)) - (k_e^p + k_{ECM}(\Theta))(u_{i-2}(t) - u_i(t)) \quad (2.3) \end{aligned}$$

where $e = (i - 1)/2$. Finally, for the last node, node I:

$$f_I = -(k_E^s + k_{ECM}(\Theta))(u_{I-1}(t) - u_I(t)) - (k_E^p + k_{ECM}(\Theta))(u_{I-2}(t) - u_I(t)) \quad (2.4)$$

Derivatives were evaluated using a backwards difference approach and yielded a set of matrix equations that can be found in full form in Appendix A.

After inverting the stiffness matrix, applying boundary conditions ($u_I(t) = u_1(t) = 0$) and solving for displacements at each time step, results were substituted back into Eq. 2.1–2.4 to solve for the isometric twitch and baseline forces. Analyses were performed for 90 twitch cycles to ensure stability and to ensure that steady state was reached.

2.3 Results and Discussion

Our experimental data showed both beneficial and deleterious effects of myofibroblasts on the contraction of engineered heart tissue (EHT). At early time points, EHT specimens containing more myofibroblasts contracted with higher baseline and twitch force; however, at later time points, when myofibroblasts had further proliferated but cardiomyocytes had not, EHT specimens with extra myofibroblasts were diminished in twitching.

The first data presented (Fig. 2.3) involved EHT specimens enriched in fibroblasts to test the myofibroblast contributions to twitch and baseline force over time. EHT specimens were produced in which 25% of the cardiomyocytes were replaced with cardiac fibroblasts. The fibroblast-enriched EHT specimens began to twitch spontaneously and coherently earlier (3 days after tissue formation) than the typical EHT without added fibroblasts (4 days). The twitch force developed by the EHT containing extra fibroblasts was significantly higher than that of the fibroblast-depleted construct on the fourth day after the formation of the construct (Fig. 2.3), whereas the baseline force was not much different. This is a reflection of the supportive contribution of fibroblasts to EHT development. On the 6th day of culture, however, the fibroblast-enriched EHT stopped twitching, yet the EHT without added fibroblasts continued to twitch and with a stronger force than that recorded on 4th day (Fig. 2.3). Additionally, on the 6th day, the baseline force of the EHT with extra fibroblasts increased to become significantly higher than that of the typical construct, indicating elevated tonic tension of the EHT (Fig. 2.3).

In another data set, twitch and baseline forces from EHT specimens were measured initially with a control tissue (no added myofibroblasts) and then over time when treated with cytochalasin D. Cytochalasin D was shown to reduce myofibroblast contribution to the mechanics of the extracellular environment. Imaging showed all sarcomeric structures (responsible for generating twitch forces) remained intact after treatment. This work [3] suggests that contractile function in cardiomyocytes are retained following application of cytochalasin D, but we cannot rule out that there existed some effect on contractile function. Results indicated and supported the hypothesis that myofibroblast play an important role mechanically in transmitting and amplifying twitch force in three-dimensional cardiac tissue at intermediate concentrations [3].

What leads to these effects? One possibility is the reduction in cardiomyocyte volume fraction as myofibroblasts proliferate plays a role. The tissue-level mechanical contribution of a species of cells can be overwhelmed by a reduction in its volume fraction. Furthermore, we hypothesized based upon these experiments that myofibroblasts in intermediate concentration serve an adaptive mechanical role by enhancing contractile function of heart tissue, and developed a computational model to further explore this.

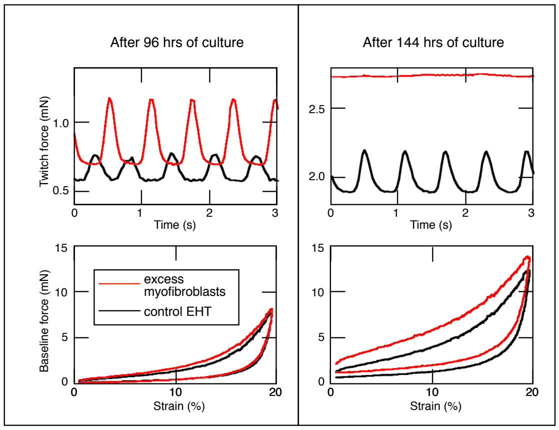

Figure 2.3: Summary of twitch and baseline forces for EHT
Summary of twitch and baseline forces for control(black) and fibroblast enriched(red) specimens. On day 4 of culture, the fibroblast enriched specimen had a much higher twitch force than the control specimen, but by day 6, the fibroblast enriched specimen stopped twitching while the control continued to twitch.

Two variables studied through our model produced significant effects on the mechanical contraction forces (twitch and baseline forces): k_{ECM}, the ECM stiffness, and Θ, the ratio of the myofibroblasts to the total number of cells. Parametric studies isolating these two variables provided insight into how myofibroblasts can affect tissue mechanics. Briefly, increasing stiffness increased force transmission and enhanced twitch production in the model. Figure 2.4 portrays the effect of increasing Θ from 0 (no myofibroblasts) to 1 (all myofibroblasts) to the overall twitch force while keeping all other parameters constant, and showed a monotonic decrease in twitch force with increasing Θ. This decrease was attributed to the volume fraction of CMs decreasing due to increase in mFB concentration. Similarly, Figure 2.5 conveys the effect on resulting twitch forces of increasing the ECM stiffness from the minimum to maximum values observed experimentally in EHT specimens. While increasing Θ produced a linear decrease in resulting twitch force, conversely, increasing ECM stiffness produced a non-linear increase in resulting twitch force. The full results of the parametric study for resulting twitch and baseline forces of varying stiffness and Θ values are described in contour plots (see Figures 2.6 and 2.7). In general, twitch force increased with stiffness and decreased with Θ, and baseline force increased with Θ and decreased with stiffness.

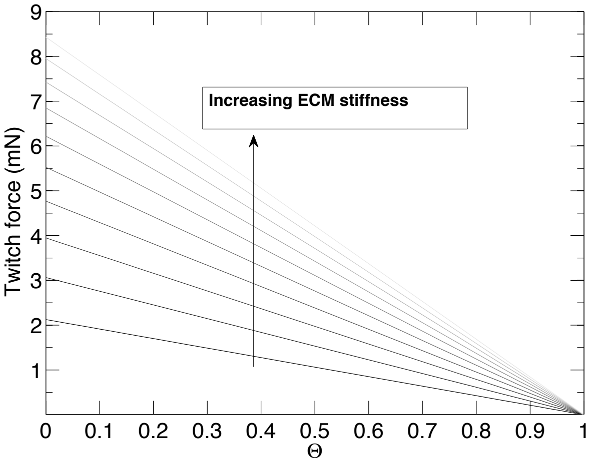

Figure 2.4: Twitch force versus mFB concentration
Resulting twitch force decreased with mFB concentration for the entire range of ECM stiffness values shown (lines show range of ECM stiffnesses).

To summarize, there exists a tradeoff with the increase of myofibroblast cell concentration. As the concentration of myofibroblasts increased, the stiffness of the tissue increased, and this enhanced the twitch transmission. This increase also caused the concentration of cardiomyocytes to decrease. Thus, at low concentrations of myofibroblasts, the incremental stiffening they provided was beneficial to twitch function, but at higher concentrations this diminished function. There is then a trade off that yields an optimal concentration for maximum twitch force function.

Another approach elaborated on this variable mapping. Because, as described previously, myofibroblasts have been shown to increase the stiffness in surrounding heart tissue, another study explored the effects of mechanical contraction assuming a relationship between Θ and ECM stiffness where $k_{ECM} = \alpha\Theta$. Therefore we examined a slice at some slope α through the twitch contour plot (Fig. 2.6) to visualize Θ versus

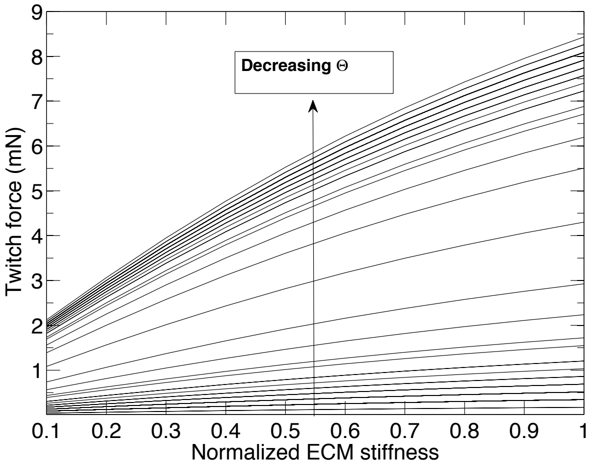

Figure 2.5: Twitch force versus normalized ECM stiffness
Resulting twitch force increased with normalized ECM stiffness for the entire range of mFB concentrations shown(lines show range of mFB concentrations).

twitch force where $k = k(\Theta)$. Because α is unknown, we explored the range of α values shown in Figure 2.8. For most cases, intermediate myofibroblast concentrations produced increased twitch forces, and higher concentrations resulted eventually in a complete cessation of contraction. We then correlated the baseline force measured over time to Θ (the concentration of contributing myofibroblasts) by converting the known area fraction to Θ for a control EHT (maximum Θ) before treatment with cytochalasin D. Figure 2.9 displays a range of possible model curves with various α values, overlaid with experimental data for Θ versus twitch force with good correlation. This evidence suggests that myofibroblasts play an important role in improving mechanical contraction in injured tissue, but proliferation, if uncontrolled, can lead to failure of contraction.

A few limitations of this study should be addressed. In a real tissue, cells form a three-dimensional network whose mechanical and steric details have a strong effect on tissue-level mechanical and electrical behavior, especially when cell concentrations are near the percolation threshold [20, 21, 5]. However, we found the one-dimensional model to be adequate for capturing the mechanical effect of myofibroblasts. This is a reasonable approximation for lower concentrations of myofibroblasts, and must be interpreted in the context of resistive percolation effects for the highest concentrations [38], as discussed below.

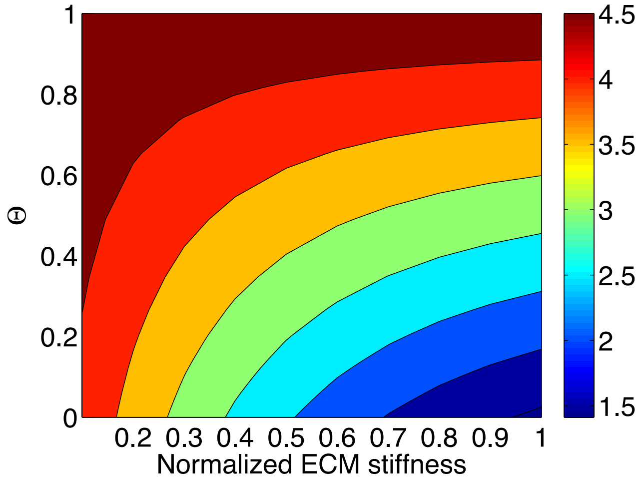

Figure 2.6: A parametric study of baseline force
A parametric study yielded resulting baseline force (mN) shown as amplitude in the contour plot with varying mFB concentration and normalized ECM stiffness. Baseline force decreased with normalized ECM stiffness, and increased with mFB concentration.

α, likely a non-linear function of Θ, was used to correlate ECM stiffness and the concentration of myofibroblasts. Refinement of predictions would be possible by calibrating this more carefully, but the qualitative trends observed here would not likely be affected as this function is expected to be monotonic in Θ.

In addition to the discussed mechanical effects, myofibroblasts can impair both heart and EHT contractile function by distorting excitatory conduction [38]. Under normal conditions the numerous fibroblasts in the heart maintain the ECM that provides the underlying structure for a continuous network of cardiomyocytes in electrical contact via gap junctions. The spread of electrical excitation in this network is organized to stimulate an orderly contraction first of the atria and then the ventricles to promote optimal pumping efficiency of the heart. Evidently, the presence of the fibroblasts in normal heart muscle does not perturb this orderly impulse conduction. Myofibroblasts can distort the propagation of the excitatory wave both by disrupting the normal interactions (gap junction formation) among the cardiomyocytes and by forming gap junctions and therefore electrical contact with the cardiomyocytes. We ignored the effect that relatively non-conductive myofibroblasts in series would have on the spread of electrical excitation by assuming the presence of a conductive medium surrounding

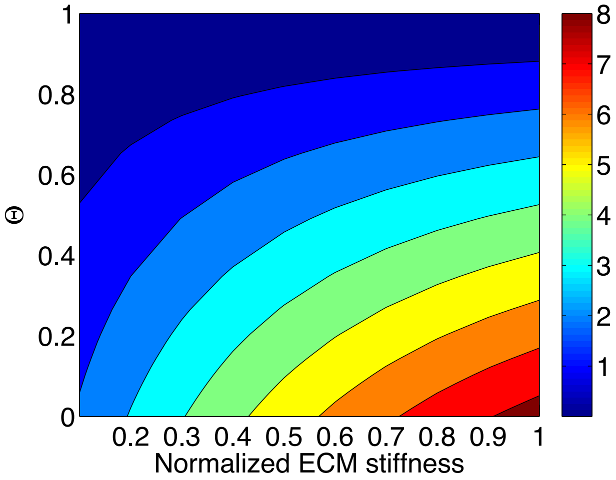

Figure 2.7: A parametric study of twitch force
A parametric study yielded resulting twitch force (mN) shown as amplitude in the contour plot with varying mFB concentration and normalized ECM stiffness. Again, twitch force increased with normalized ECM stiffness, and decreased with mFB concentration.

the string of cells. However, delineating the influence of mechanical stretch versus mechanoelectrical coupling is an important and discussed more in Chapter 3.

The combination of the mechanical and electrical functional degradation could be responsible for arrhythmias and conduction problems in the heart. Tissue constructs provide a promising platform for understanding these interactions.

Conclusion

We developed simplified experimental and theoretical models that give insight into interactions between myofibroblasts and cardiomyocytes. Experiments suggested that myofibroblasts are initially mechanically beneficial to the function of heart tissue during wound healing, but at high concentrations ultimately cause mechanical obstruction. Further insight from the computational model showed two parameters to be central to positive and deleterious effects of myofibroblasts on twitch: ECM stiffness, k_{ECM}, and ratio of myofibroblasts to total cells, Θ. Separately, increasing k_{ECM} increased twitch force, while increasing Θ decreased twitch force. Assuming

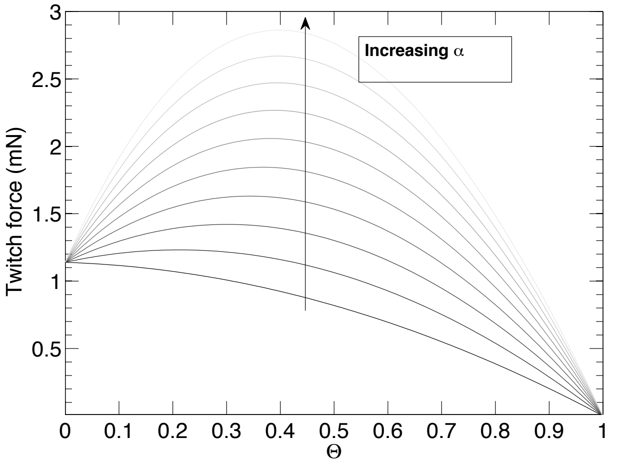

Figure 2.8: Twitch force versus mFB volume fraction for increasing α values
A relationship between ECM stiffness and Θ was assumed where $k_{ECM} = \alpha\Theta$. Twitch force versus mFB volume fraction for increasing α values (shown in lines) resulted in an initial increase in twitch force with mFB concentration followed by a decrease.

a relationship between the two, $k_{ECM} = \alpha\Theta$, where α is a proportionality constant, the model predicted intermediate concentrations of myofibroblasts to increase twitch force optimally. These models and data suggest that myofibroblasts are important in improving contraction in injured heart tissue, but proliferation, if uncontrolled, can lead to failure of contraction.

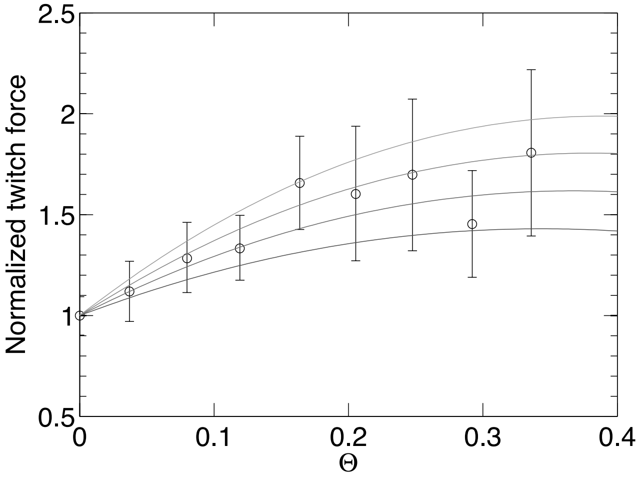

Figure 2.9: Twitch force versus mFB volume fraction compared to experimental data Normalized twitch force (normalized to begin at 1) versus mFB volume fraction for a range of α values (shown as lines) was compared to experimental twitch force data. Experimental data was obtained by treating EHT with cytochalasin D to decrease mFB contribution.

Chapter 3

Statistical electrophysiologic bounds and estimates for conduction velocity in idealized fibrotic myocardium

3.1 Introduction

Cardiomyocytes (CMs) and fibroblasts make up the majority of cells in healthy myocardium. While cardiomyocytes are primarily responsible for the mechanical contraction, fibroblasts are responsible for maintaining the extracellular matrix and tissue compliance. Under certain pathological conditions though, such as hypertension or infarction, this delicate balance can be disrupted [27].

In responding to such injury, fibroblasts convert to myofibroblasts (mFBs), a larger and more contractile phenotype intermediate between a fibroblast and a smooth muscle cell. In contrast to normal fibroblasts, the mFBs express α-smooth muscle actin (α-SMA), which is essential to its increased contractility, but, unlike a smooth muscle cell, it retains its capacity for secreting collagen. Both contractile and collagen synthetic capabilities are necessary for wound healing. Nevertheless, mFBs can produce a pathological condition, fibrosis (the formation of excess fibrous connective tissue), in a variety of organs, e.g., lung, kidney, liver, and heart. Although this adaption preserves the overall functioning of the heart, it can lead to altered electrical impulse propagation and possibly produce arrhythmias [27].

Understanding how mFBs alter electrical impulse conduction in the heart is important in developing clinical strategies for treatment. Continuum approximation using the bidomain equations [1] is widely used to describe cardiac electrophysiology impulse spread [33]. Others have combined experimental estimates of cellular geometry with cellular ionic models to study cardiac electrophysiology from the cellular level [29]. In this work, we have paralleled the approach of Xie et al. [39, 38, 37] by developing a discrete computational model formulated at the cellular level taking into account individual CMs and mFBs. Cells were connected by gap junctions to yield the pattern of impulse spread as modulated by the presence of mFBs. To expand on these studies, we have compared two models for CMs, the Luo-Rudy (LR1) [16] and Luo-Rudy Dynamic (LRd) [8], with the mFBs following a two-parameter passive model from MacCannell et al. [2]. LR1 was a first generation ionic cell model while LRd extended to a more detailed and dynamic model with pumps, exchangers, and more detailed cellular calcium information. In both cases, mFBs slowed conduction velocity, as expected, and at a percolation threshold either completely blocked conduction or caused spontaneous excitation by raising the surrounding CMs resting potential. Results followed closely to the rigorous bounds of effective conductivity developed for an idealized passive random heterogeneous material representative of fibrotic myocardium [31].

3.2 Methods

3.2.1 Tissue and cellular electrophysiology

At the level of cells, the discrete approach of Xie et al. [39, 38, 37] was applied in which the time rate of change of the membrane voltage V of a subject cell, a CM or mFB, is a function of the membrane capacitance C_i, the membrane current I_{ion}, the membrane voltages V^k of the K cells in contact with the subject cell, and the gap junction conductances G^{ik} with each of these cells:

$$C^i \frac{dV^i(t)}{dt} = -I_{ion} + \sum_{k=1}^{K} G^{ik}(V^k(t) - V^i(t)). \tag{3.1}$$

For CMs, I_{ion} followed Luo-Rudy "LR1" [16] or "LRd" model [8, 15] based on data from membrane action potential in guinea pig ventricular cells. For mFBs, I_{ion} followed a two-parameter passive model of MacCannell et al. [2],

$$I_{ion} = G_f(V - E_f) \tag{3.2}$$

where G_f is the membrane conductance of a mFB and E_f is the resting potential of a mFB.

Spread of excitation within a tissue was modeled by studying an idealized CM (red) and mFB (yellow) network, with both parallel and series connections between mFBs and CMs (e.g. Fig. 3.1) and with insulated boundary conditions. Conductivity was studied as a function the of mFB volume fraction, Θ. Random patterns of varying volume fractions of CMs and mFBs (from all CMs to all mFBs) were generated and conductivity results were studied to understand their effects on EHT. Solution of Eq. 3.1 over such a domain involved finite difference simulations with alternating time steps for the membrane current and gap conduction terms, following the method of Qu et al. [26]. In the example in Fig. 3.1, with mFBs connecting end-to-end with CMs and pacing on its left boundary, effective conduction ceases beyond a critical percolation threshold either because of break-up of the leading wave or because of spontaneous independent contractions. The theoretical percolation threshold is the critical volume fraction at which, when adding random conducting squares into a non-conducting medium, a continuously connected network forms and conductivity from end to end occurs. If assuming mFB conductivity is very low, the theoretical percolation threshold for mFB volume fraction in these simulations would occur at 0.33 [4]. Xie et al. [39, 38, 37] have shown that the threshold in these simulations, is a strong function of the electrical connections between mFBs and CMs.

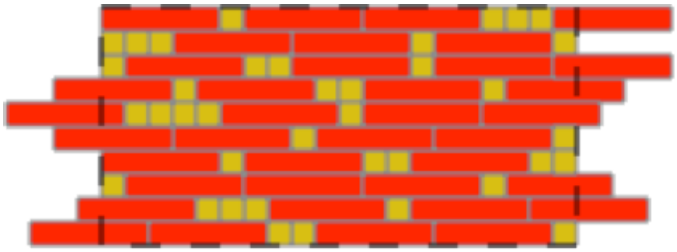

Figure 3.1: Schematic of a typical simulation
Schematic of a typical simulation with CMs in red and mFBs in yellow. Specimen is stimulated along the left edge and the impulse travels across the tissue. The voltage is studied as modulated by the mFBs.

3.2.2 Effective conductivities

Heterogeneous materials are materials that are composed of multiple phases, either different materials (composites) or the same material in different states (polycrystal) [31]. It is difficult to quantify properties for this category of materials. Under certain conditions, including when the microscopic length scale is much smaller than the macroscopic length scale, and the material is ergodic, meaning averaging over all realizations of a random system is the same as averaging over one realization of that system, then it can be treated as a continuum with effective properties on the macroscopic scale for classical analysis. Because of the difficulty of determining exact effective properties for random heterogeneous media, effective properties are studied in the form of rigorous bounds. Here we are interested in EHT, composed of two different materials, with conductivities of σ_1 and σ_2. Using microstructure information, one can develop rigorous bounds for these effective properties. The more information quantified in the microstructure, the narrower the bounds. Methods are for idealized passive materials. EHT is an active material, and theory was used for context and further insight into simulation results.

In the simplest form (one-point bounds), only volume fractions of each material are considered (Θ_1 and Θ_2) [31]. The arithmetic average (Eq. 3.3) tends to overestimate the effective property, thus becoming the upper bound, while the harmonic-average (Eq. 3.4) tends to underestimate the effective property to make the lower bound. This is because the arithmetic average represents exactly a layered composite, depicted in Fig. 3.2A, whereas the harmonic average corresponds exactly to the composite in the perpendicular direction of this same system (Fig. 3.2B). In general, random heterogeneous materials effective properties lie somewhere between these one-point bounds.

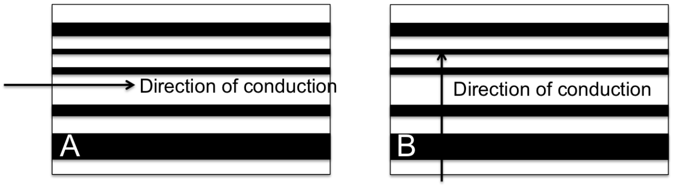

Figure 3.2: Description of one-point bounds equations
Description of one-point bounds equations where the upper limit is the arithmetic average(A) and the lower limit is the harmonic average(B).

$$\sigma_U = \sigma_1\Theta_1 + \sigma_2\Theta_2 \tag{3.3}$$

$$\sigma_L = \frac{\sigma_1}{\Theta_1} + \frac{\sigma_2}{\Theta_2} \tag{3.4}$$

Correlation functions are used to describe the statistical microstructure of a material. Take, for example, a two phase medium, shown in Fig. 3.3. The one-point correlation function (S1) would be equal to the fraction of times a randomly placed point lands in one phase, say the white phase. This would then approach the volume fraction as the number of points placed goes to infinity. Similarly, the two-point correlation function (S2) is obtained by randomly throwing a line (radius r) onto the planar section and determining the fraction of times the two end points land in the white phase. S2, a function of r, then shows how these two phases are correlated in the system. Finally, the three-point correlation function (S3) is determined by the fraction of times random triangles with vertices r, s, and t, lie inside of the white phase. Further microstructure information thus leads to more rigorous bounds. The following sections develop equations used to study the effective conductivity bounds for idealized EHT [31].

Two-point bounds

Here we assumed isotropic phases and thus, each phase was characterized by the scalar conductivity, σ. Hashin and Shtrikman developed the best possible bounds given only

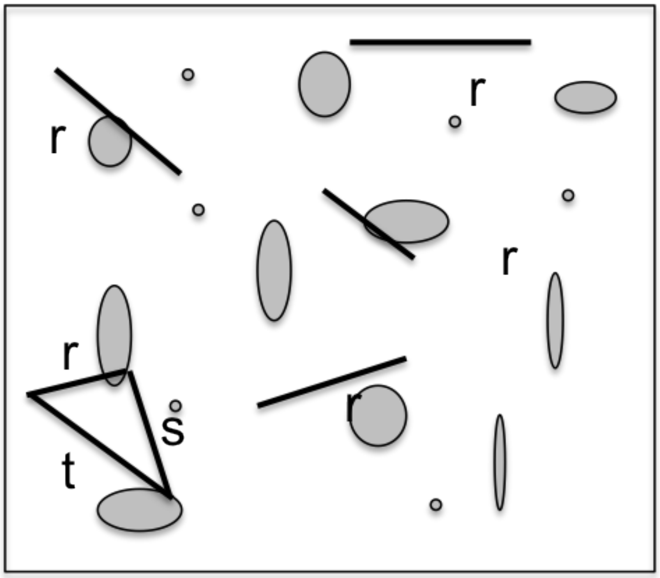

Figure 3.3: Schematic of formulation of correlation functions
Schematic of formulation of correlation functions for describing material microstructure and developing effective conductivity bounds.

volume fraction information by incorporating two-point probability functions [10]. These are considered two-point bounds, but because for isotropic media, S2 only depends on endpoints of the function, only volume fractions are needed. Below are the d-dimensional Hashin-Shtrikman bounds for conductivity for a two-phase, isotropic media with $\sigma_2 \geq \sigma_1$:

$$\boldsymbol{\sigma_L^{(2)}} = \langle \boldsymbol{\sigma} \rangle - \frac{\Theta_1 \Theta_2 (\sigma_2 - \sigma_1)^2}{\langle \tilde{\boldsymbol{\sigma}} \rangle + (d-1)\sigma_1} \tag{3.5}$$

and

$$\boldsymbol{\sigma_U^{(2)}} = \langle \boldsymbol{\sigma} \rangle - \frac{\Theta_1 \Theta_2 (\sigma_2 - \sigma_1)^2}{\langle \tilde{\boldsymbol{\sigma}} \rangle + (d-1)\sigma_2} \tag{3.6}$$

where

$$\langle \boldsymbol{\sigma} \rangle = \sigma_1 \Theta_1 + \sigma_2 \Theta_2 \tag{3.7}$$

and

$$\langle \tilde{\boldsymbol{\sigma}} \rangle = \sigma_1 \Theta_2 + \sigma_2 \Theta_1. \tag{3.8}$$

These equations can be expanded for use in macroscopically anisotropic composite medium consisting of two isotropic phases (generalized Hashin-Shtrikman bounds) when $\sigma_2 \geq \sigma_1$:

$$\boldsymbol{\sigma}_{\boldsymbol{L}}^{\mathbf{(2)}} = \langle \boldsymbol{\sigma} \rangle + (\sigma_1 - \sigma_2)^2 \boldsymbol{a}_{\mathbf{2}} \cdot [\sigma_1 \boldsymbol{I} \frac{\sigma_1 - \sigma_2}{\Theta_2} \boldsymbol{a}_{\mathbf{2}}]^{-1} \tag{3.9}$$

and

$$\boldsymbol{\sigma}_{\boldsymbol{U}}^{\mathbf{(2)}} = \langle \boldsymbol{\sigma} \rangle + (\sigma_2 - \sigma_1)^2 \boldsymbol{a}_{\mathbf{2}} \cdot [\sigma_2 \boldsymbol{I} \frac{\sigma_2 - \sigma_1}{\Theta_1} \boldsymbol{a}_{\mathbf{2}}]^{-1} \tag{3.10}$$

where $\boldsymbol{a}_{\mathbf{2}}$ is the two-point tensor that is derived using contrast expansion. For statistically anisotropic microstructures in which the micro surfaces have ellipsoidal symmetry, $\boldsymbol{a}_{\mathbf{2}}$ is give by:

$$\boldsymbol{a}_{\mathbf{2}} = -\Theta_1 \Theta_2 \boldsymbol{A}^{*} \tag{3.11}$$

where $\boldsymbol{A}^{\boldsymbol{*}}$ is the polarization tensor for an ellipsoid and dependent on the short and long axis lengths. For spheres, $A_1^* = A_2^* = A_3^* = \frac{1}{3}$, and for needle shaped inclusions, $A_1^* = A_2^* = \frac{1}{2}$ and $A_3^* = 0$.

Three-point bounds

By adding in more detailed microstructure information in the form of a three-point correlation function (S3), one can further narrow the bounds for effective conductivity. Bounds for d-dimensional two-phase isotropic media are:

$$\boldsymbol{\sigma}_{\boldsymbol{L}}^{\mathbf{(3)}} = \langle \boldsymbol{\sigma} \rangle - \frac{\Theta_1 \Theta_2 (\sigma_2 - \sigma_1)^2}{\langle \tilde{\boldsymbol{\sigma}} \rangle + (d-1) \langle \boldsymbol{\sigma}^{\mathbf{-1}} \rangle_{\zeta}^{-1}} \tag{3.12}$$

and

$$\boldsymbol{\sigma}_{\boldsymbol{U}}^{(\mathbf{3})} = \langle\boldsymbol{\sigma}\rangle - \frac{\Theta_1\Theta_2(\sigma_2-\sigma_1)^2}{\langle\tilde{\boldsymbol{\sigma}}\rangle + (d-1)\langle\boldsymbol{\sigma}\rangle_\zeta} \tag{3.13}$$

where

$$\langle\boldsymbol{\sigma}\rangle_{\boldsymbol{\zeta}} = \sigma_1\zeta_1 + \sigma_2\zeta_2, \tag{3.14}$$

and $\zeta_1 + \zeta_2 = 1$. These depend not only on volume fraction information, but also the three-point microstructure parameter ζ which has been derived for several geometries including cubical cells using contrast expansion,

$$\zeta_2 = 0.11882\Theta_1 + 0.88118\Theta_2. \tag{3.15}$$

These rigorous bounds were developed to compare the statistical electrophysiologic conduction velocity estimates to the idealized cases described for fibrotic myocardium.

3.3 Results

Statistical electrophysiologic simulations with varying volume fractions of CMs and mFBs were studied. Random patterns of distributed mFBs and CMs were studied from 0 to 1 mFB volume fraction to understand their effect on conductivity in EHT. In Figure 3.4 markers represent normalized conductivity of the simulations where individual CM ionic currents were modeled by the Luo-Rudy Dynamic (LRd) [8], while Figure 3.5 shows resulting conductivities when CMs were modeled by Luo-Rudy 1 (LR1) [16]. All results were normalized to have a maximum conductivity of 1.

These trends can be understood in the context of the bounds described in the chapter. Rigorous bounds were developed for effective conductivity for one-point, two-point, three-point, two-point anisotropic, and three-point anisotropic cases. Solid lines show bounds of normalized effective conductivity for each of these cases in Figure 3.6. For

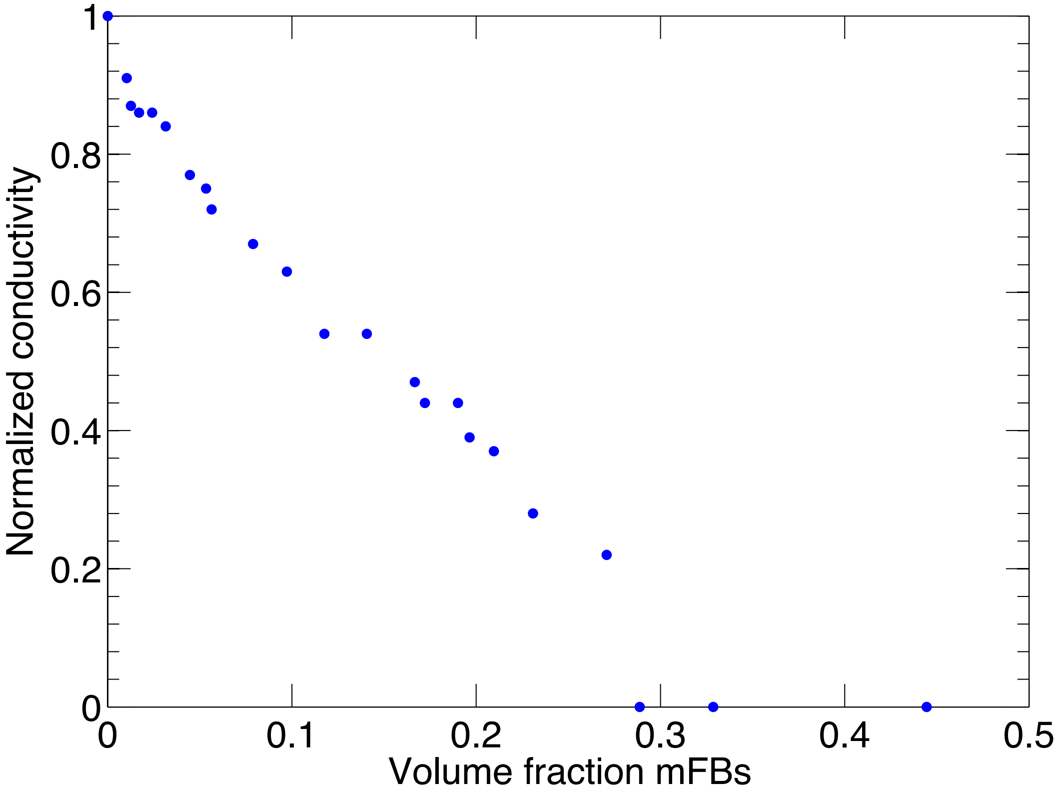

Figure 3.4: Resulting normalized conductivity for simulation results for LRd Resulting normalized conductivity for simulation results using the Luo-Rudy Dynamic model shows a gradual decrease in conductivity with increased mFB volume fraction until about 0.28 when conduction is completely blocked.

anisotropic cases, ellipsoids were assumed to represent CMs within a sheet of mFBs with varying volume fractions. The theoretical percolation threshold (line in Fig. 3.6), is very close to the measured simulation percolation threshold in both models.

Conductivity decreased with increased mFB volume fraction until a critical electrical percolation threshold caused conduction to completely cease. Conduction failed (conductivity was 0) for one of two reasons. Either the mFB blocked conduction from reaching the opposite end of the tissue, or the mFBs increased the resting potential of the surrounding CMs and caused spontaneous excitation to occur. This percolation was determined by the divergence of the estimated conductivity of the simulation from its one-point bounds. The peaks in Figure 3.7 for LRd and LR1 yield the volume fraction of mFBs for which percolation occurs.

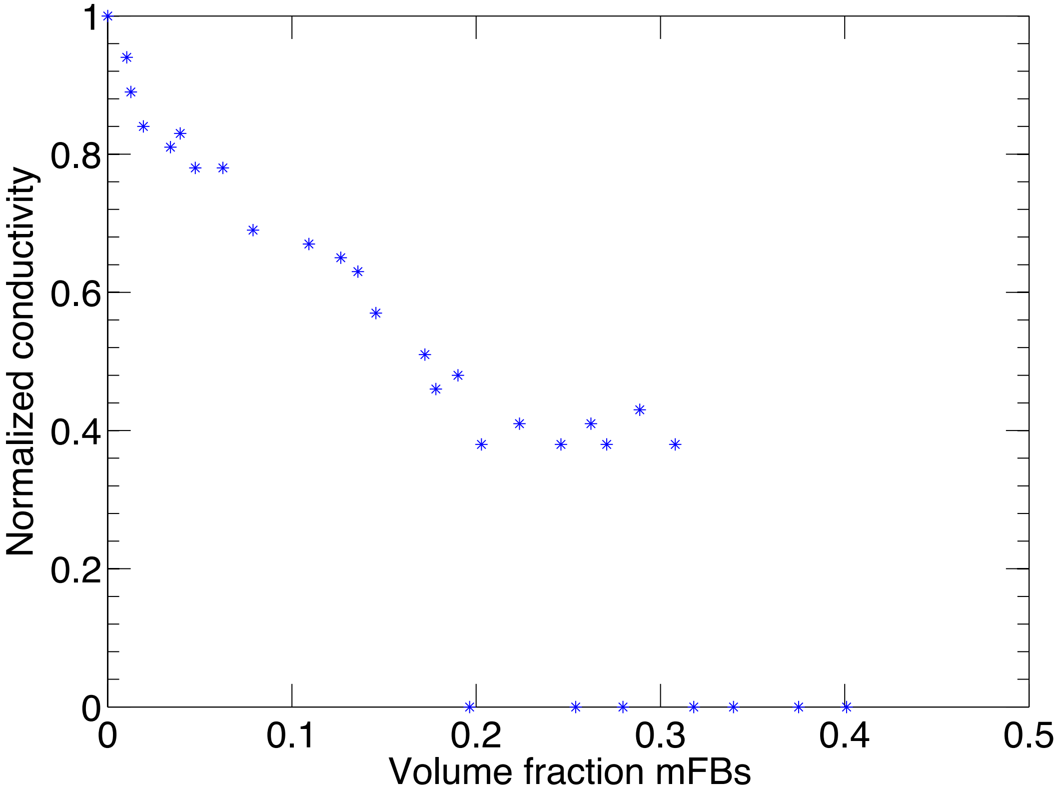

Figure 3.5: Resulting normalized conductivity for simulation results for LR1 Resulting normalized conductivity for simulation results using Luo-Rudy first generation model shows decreased conductivity for increasing mFB volume fraction until about 0.2 when data becomes noisy and then completely dropped off.

EHT was stimulated on the left side, and voltage was monitored throughout the tissue. Conduction velocity of each case was determined by observing the voltage at the opposite end of the tissue (right side, away from stimulation). The time elapsed from the initial external stimulus to when the voltage exceeded 5 mV on the opposite side was used to calculate the conduction velocity. Anomalies occurred in this value when spontaneous excitation caused cells away from the intended point of external stimulation to depolarize and produce a secondary impulse. The apparent conduction velocities for LRd decreased and eventually went zero for high mFB volume fractions, while the apparent conduction velocities for LR1 decreased steadily and then increased to very large values near this electrical percolation (Fig. 3.8). The two models failed near the same values, but in very different modes. While LRd slowed conduction

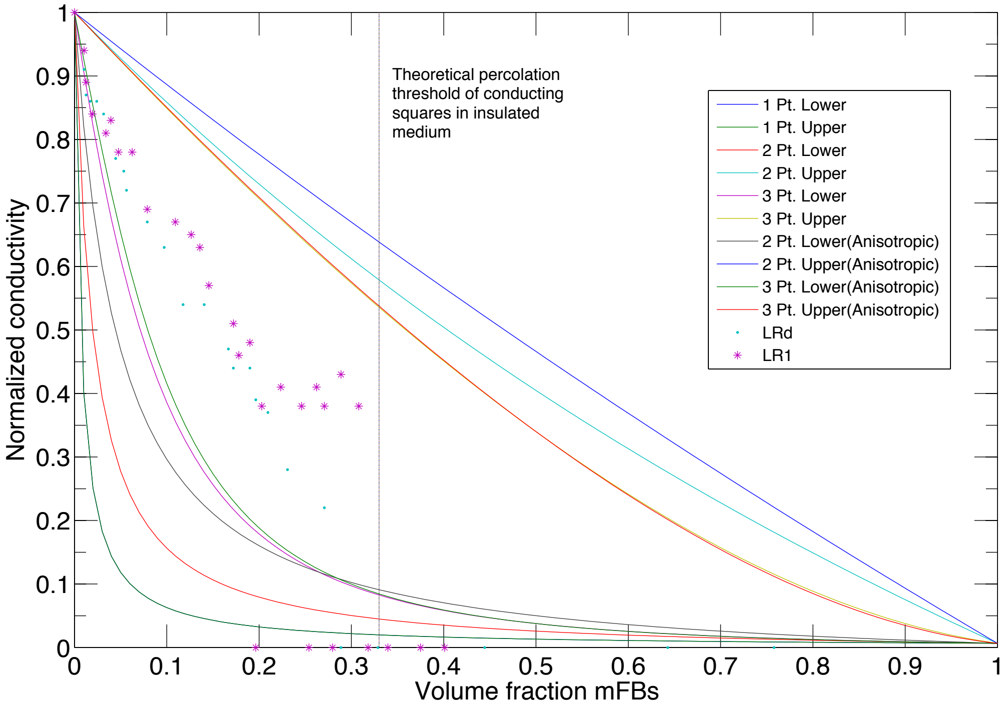

Figure 3.6: Simulation results in context of effect conductivity bounds
Normalized conductivity for both LR1 and LRd models follow in the middle of the effective conductivity bounds established for a passive random heterogeneous material until a critical percolation threshold where conduction fails. The line shows predicted theoretical percolation of conducting squares in a non-conducting medium.

gradually due to mFBs, LR1 failed due to autonomous excitation caused by mFBs increasing surrounding CMs resting potential(Fig. 3.9).

3.4 Discussion

Results showed decreased conductivity with increased mFB volume fraction leading to a percolation where the conductivity went to zero. When compared to the two-point bounds, the simulation results followed along the upper bounds and suddenly dropped off when mFBs volume fraction approached a percolation(Fig. 3.6). The two models for CM ionic current studied were the LR1 first generation model, and the

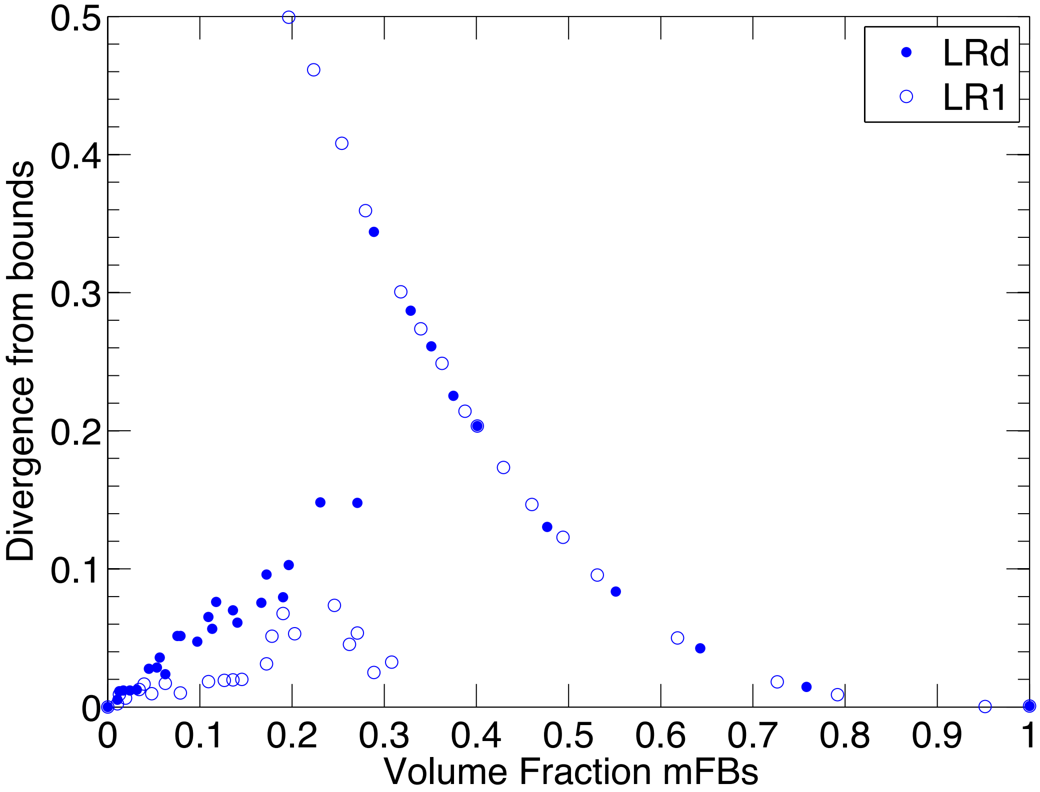

Figure 3.7: Divergence from bounds
To determine the percolation of each data set, the conductivities were compared to the two-point upper bounds. The divergence from this bound shows a peak where failure first occurs (0.2 for LR1 and 0.28 for LRd).

LRd dynamic model that was expanded to include pumps, exchangers, as well as more detailed cellular calcium information. For the LRd model, the decreased conductivity was a gradual and smooth drop off at a mFB volume fraction of about 0.28(Fig. 3.4). In contrast, the LR1 model decreased gradually at first, but became bistable at a volume fraction of approximately 0.2 and then dropped off completely(Fig. 3.5). Bounds were calculated for an idealized passive random heterogeneous materials with two materials and two conductivities representing idealized fibrotic myocardium. Results followed closely with the upper bounds until percolation prevented conduction where conductivities jumped down to the lower bounds. This could be attributed to the active nature of the CMs and the passive nature of the mFBs. Initially, at low mFB volume fractions, CMs are dominant and therefore conductivities are more active and

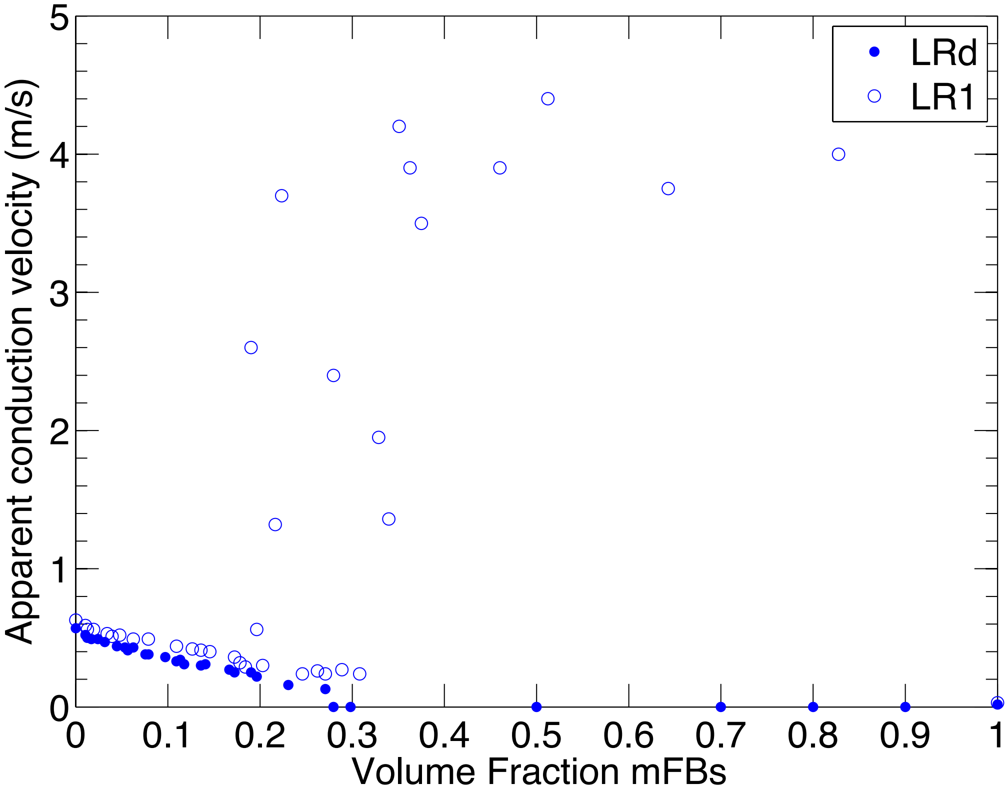

Figure 3.8: Apparent conduction velocity
Apparent conduction velocity was determined by the elapsed time from initial stimulation to the time when the opposite end excited. The large values of apparent conduction velocity indicate spontaneous excitation occurred in the simulations using LR1 after the percolation threshold.

follow along the upper bounds. After a critical percolation threshold, CMs no longer form a continuos network, and the passive nature of mFBs dominate. The interactions between the two cell types are also apparent in LR1, near the percolations threshold, when results are unstable due mFBs raising resting potential of surrounding CMs and causing autonomous excitation.

The percolation threshold of the simulation was determined by studying the divergence of the conductivities from the idealized one-point bounds. The percolation threshold was indicated by a jump in this quantity(Fig. 3.7). In all cases, LRd failed when the network of mFBs completely blocked conduction and thus, failed at a higher

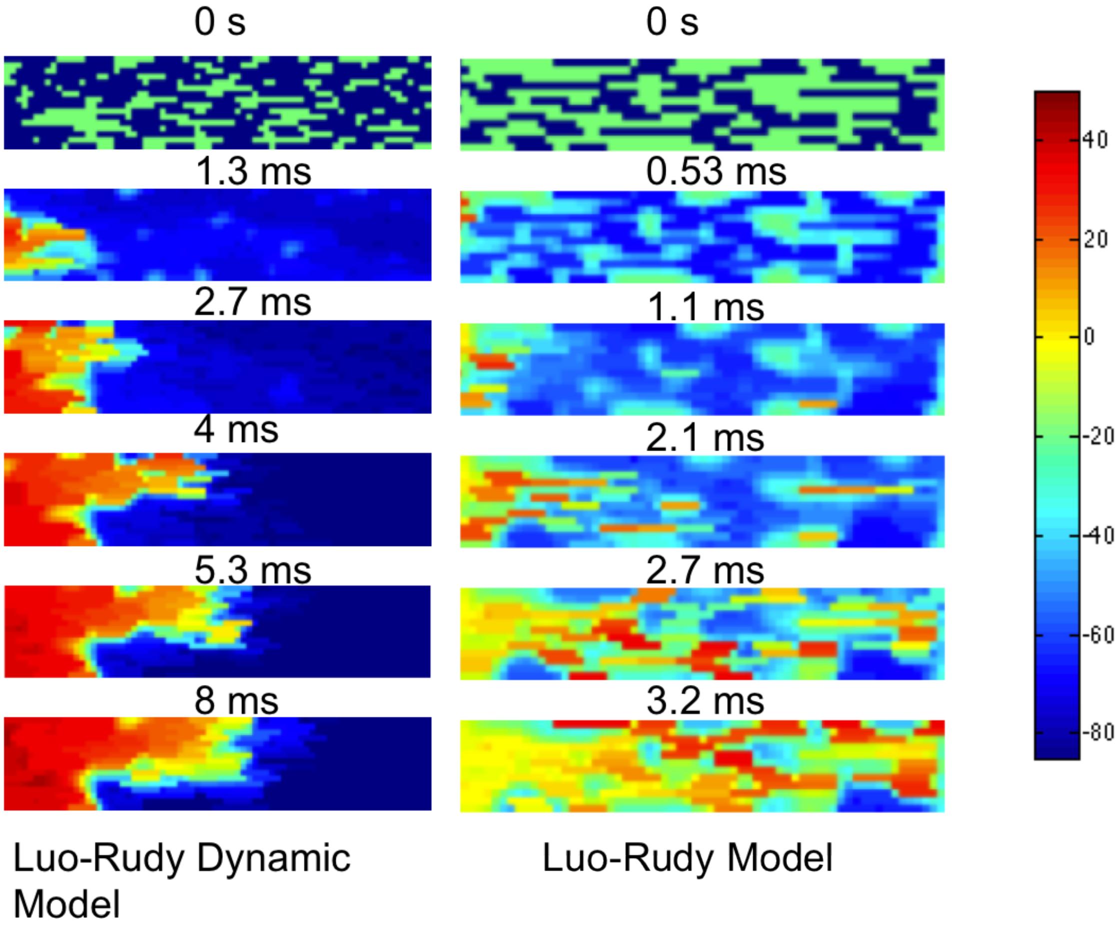

Figure 3.9: Failed conduction time course
Conduction failed either passively in the case of LRd, or actively in the case of LR1. LRd failed due to conduction being completely blocked whereas LR1 failed due to spontaneous excitation in most cases.

mFB volume fraction than LR1. This threshold occurred sooner for the LR1 model because of the models susceptibility to autonomous excitation.

Spontaneous excitation was evident in apparent conduction velocities(Fig. 3.8). Conduction velocity was calculated by determining the time elapsed from the initial external stimulation to the time the voltage increased above 5 mV at the opposite end of the tissue. If stimulus traveled uniformly across the tissue, then the conduction velocity would be this elapsed time divided by the total length of the tissue. This was true for the LRd studies. With the LR1 model though, mFBs increased the resting potential of nearby CMs causing individual cells or cell groups throughout the tissue to autonomously excited and produce secondary stimulus from locations other then the intended external stimulus location (left edge of the tissue). Therefore the time elapsed from the input external stimulus and excitation at the other end of the tissue yielded an apparent conduction velocity that was much higher than the expected value. Figure 3.8 conveys apparent conduction velocities where simulations with LR1 increased to a large value at percolation and LRd decreased to zero. A time series of voltage for several time steps shows LRd failed conduction due to a blocking of mFBs while LR1 failed due to a raised resting potential from the mFBs (Fig. 3.9). Differences in failure mode between the two models highlight the difference between passive, and active effects of mFBs in the shutting down of conduction. LRd failed passively from mFBs by a complete blockage of conduction, and in contrast, LR1 failed actively from mFBs by the onset of spontaneous contraction.

It is important to understand these results in the context of the mechanical simulation results from Chapter 2. In small concentrations mFBs improved contraction, and the electrophysiologic simulations show only a slightly decreased conduction velocity. This would suggest that mFB concentrations up to the electrical percolation threshold might in fact improve contraction with little effect on electrical impulse propagation. However, both electrical and mechanical effects can eliminate the contractile function of EHT at high mFB volume fractions.

While this model studied the two-dimensional effects of mFB on electrical function in EHT, it is important to note that in EHT cells form a continuous three-dimensional network important for replication of the mechanical and electrical biophysics of natural myocardium. This two-dimensional simplification was adequate for capturing the overall effects of mFBs on tissue electrophysiology, but future three-dimensional studies would yield more accurate results. Additionally, both mechanical and electrical modulation of EHT by mFBs are ultimately important, and this will be discussed further in Chapter 5.

3.5 Conclusions

Comparison of statistical electrophysiologic conductivity bounds and conduction velocity estimates for idealized fibrotic myocardium yielded insight into the electrical interactions of mFBs and CMs. At low volume fractions, mFBs reduced conduction velocity minimally, in a way that paralleled the effective conductivity for the upper two-point bound of a passive heterogeneous material. However, beyond a critical percolation threshold, the effects were profound and conduction completely failed, either due to the onset of spontaneous excitation (active percolation) or the complete blockage of conduction (passive percolation). Results also showed differences in the effects of mFBs on the two implemented CM ionic models (Luo-Rudy 1 versus Luo-Rudy Dynamic). Future studies should be done by varying tissue model properties (i.g. gap junction conductances, mFB conductance, and membrane capacitance), as well as properties internal to the CM ionic models, to understand how these effect excitability of the two models differently. Results show that the negative effects on conduction appear most dramatically at mFB concentrations beyond a percolation threshold. Taken with the results of Chapter 2, this suggests that low to moderate concentrations of mFBs are beneficial to contractile function. Results support the idea of the early stages of fibrosis providing advantageous contractile effects to the heart tissue without significant degradation of electrical function. Studies by Thompson et al. indicated mechanical coupling between mFBs and CMs played an important role in slowed conduction in fibrotic monolayers [30], and this limitation of the model will be addressed in future studies. Furthermore, the trade-off between electrical and mechanical percolation effects in two-dimensions will be the focus of Chapter 5.

Chapter 4

Observations of cardiomyocyte depolarization and conduction velocity estimates

4.1 Introduction

In responding to a wound, fibroblasts convert to myofibroblasts (mFBs), a larger and more contractile phenotype intermediate between a fibroblast and a smooth muscle cell. In contrast to the normal fibroblast, the mFBs expresses α-smooth muscle actin (α-SMA), which is essential to its increased contractility, but, unlike a smooth muscle cell, it retains its capacity for secreting collagen. Both contractile and collagen synthetic capabilities are necessary for wound healing. Nevertheless, mFBs can produce a pathological condition, fibrosis (the formation of excess fibrous connective tissue). Although some level mFB function is adaptive and preserves the overall functioning of the heart after myocardial infarction and possibly also in hypertension, it can disrupt electrical impulse propagation and ultimately lead to arrhythmias [27].

Studies have shown that in two-dimensional cell culture, gap junction coupling exists between CMs and mFBs and can alter impulse propagation. Conduction velocity was shown to decrease with increased mFB concentration for both cases in which mFBs and CMs were in series and in parallel [9, 22]. Monolayers of cocultured mFBs and CMs also showed a decrease in conduction with increased mFB concentration as well as indications that mechanical interactions plays an important role in conduction modulation [30]. With little data on the heterogeneous cell coupling in native myocardium though, the applicability of these results in natural myocardium is uncertain [14].

Understanding how mFBs alter electrical impulse conduction in the heart is important in developing clinical strategies for treatment. We have used well characterized three-dimensional tissue constructs, engineered heart tissue (EHT), to study these effects. The experimental model consists of EHT assembled from embryonic CMs and containing defined fractions of mFBs randomly distributed throughout the tissue. EHT is three-dimensional and replicates the behavior of natural heart tissue well [3, 7], while still allowing the flexibility to control specific parameters, such as cell volume fractions, collagen concentration, and boundary conditions. While conduction velocities have been studied in one-dimensional culture [27] and in whole hearts [6], our work extends beyond earlier studies in its ability to investigate the effects of randomly dispersed mFBs on impulse propagation in a more realistic three-dimensional environment. Here, by controlling the initial, and measuring the current mFB volume fraction in EHT we have shown conduction velocity decreases with increased mFB volume fraction in these preliminary studies.

4.2 Methods

4.2.1 EHT Preparation

EHT specimens were prepared as described previously [7] by isolating cardiomyocytes from 10-day-old chicken embryos, and suspending the cells (approximately 1.4 million/ml, final concentration) in Type I rat tail collagen, DMEM with 10% FBS, and 4% chicken embryo extract. The mixture was poured into a mold and placed in a 37°C CO_2 incubator producing a loose collagen gel in which cells were randomly distributed. Within 5 days the cardiomyocytes began contracting independently and experiments were conducted between days 5 and 17 days.

Because the fibroblasts adhere more strongly than the CMs to plastic cell culture dishes, they were separated by allowing the primary cell suspension to rest in a culture dish for a defined time period. Two sets of EHT were studied. The first was a control and followed the protocol described previously [7]. In the second set of specimens, 20% of the CMs were removed and replaced with mFBs. These two systems were then studied over time to compare conduction velocity estimates in each. The control specimens were tested 6, 8, and 17 days after preparation, and mFB enhanced specimens were tested 5 and 7 days after preparation.

4.2.2 Calcium transient measurements

Calcium transients were measured using Fluo-2 (TEFlabs, Austin, TX) with an excitation/emission of 488/515 nm. This fluorescent indicator of bound calcium in the cell changes intensity with calcium concentration, as can be seen from the raw data from a single cell calcium transient in Figure 4.1). Experiments were preformed on a Zeiss LSM 510 scanning confocal microscope using a 470 nm LED for excitation with a 10x objective, and images were captured using a pco.edge sCMOS camera (Kelheim, Germany) with speeds from 110-120 frames/second (Fig. 4.2A-C). Tissues were removed from metal spacer bars and placed on glass bars with small wires attached during imaging. These wires were used to stimulate the tissue in the small contacting area. Specimens were stimulated with a Grass SD9 Stimulator with a frequency of approximately 1 Hertz. Voltage was determined by starting low (less than 1 volt) and increasing until the specimen followed the stimulus (usually around 5 volts). Frequency for the stimulation and camera frame rate were determined by a timing circuit(Fig. 4.3). Because tissues spontaneously contract, it was sometimes difficult to ensure the EHT was following the stimulus until images were post-processed.

Because of the high speed impulse propagation (about 5 cm/sec) and limitations on light and camera speed, the impulse traveled too fast to capture a conduction velocity by mapping over the entire specimen. Instead an innovative method was developed to determine the conduction velocity of specific groups of cells within the tissue. In general, the system was synced so that the tissue was stimulated simultaneously with the triggering of the camera to record (Fig. 4.2) by a controlling timing circuit(Fig. 4.3). A sequence of images was acquired of a group of cells near the point of simulation, and then another sequence was taken of the same group of cells with the stimulation point on the opposite end of the tissue (Fig. 4.4). This was done for several impulses and three times for each direction to ensure repeatability. Then the time difference

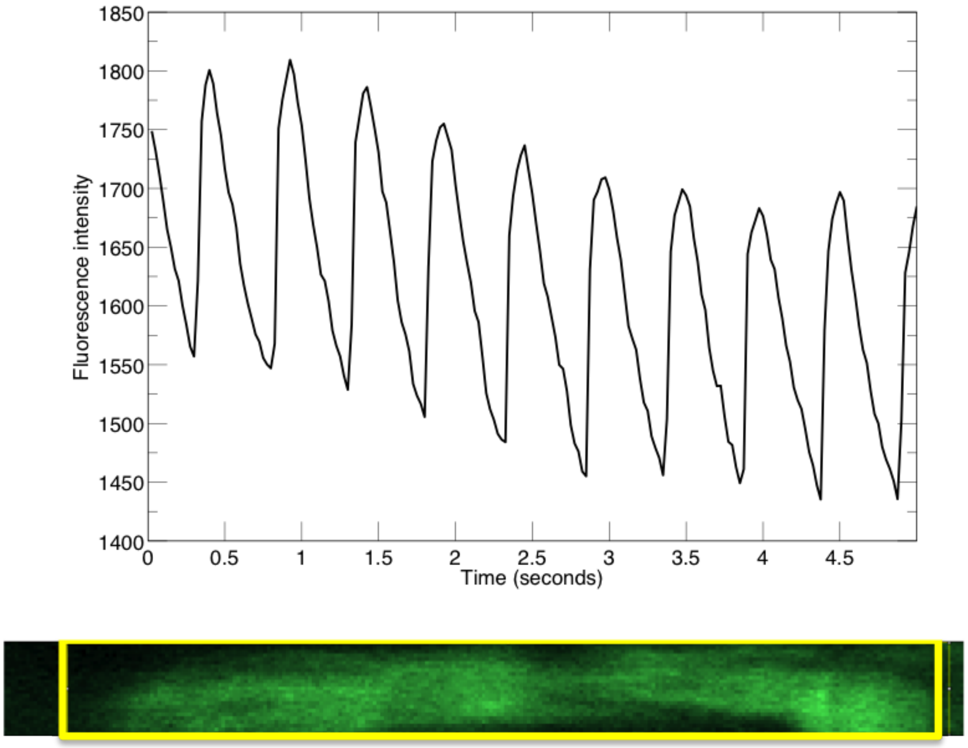

Figure 4.1: Single cell calcium transient
Raw data from a single cell calcium transient measurement of fluorescence intensity over time was acquired. Cells were stained using Fluo-2 (TEFLabs), and data was obtained with a Zeiss LSM 510 scanning confocal microscope using a 10x objective. Temporal resolution was 24 ms.

between the two calcium transient peaks (Δt), was the time it took for the impulse to travel from one end of the tissue to the other end, yielding conduction velocity. Multiple positions on the tissue were evaluated and compared.

4.2.3 Immunofluorescence volume fraction analysis for CMs and mFBs

Samples were fixed using 4% paraformaldehyde at each data point to determine volume fractions of CMs and mFBs. Previously described methods of immunofluorescence imaging and image analysis were used to determine CM and mFB volume fractions [3]. For titin labeling, specific monoclonal antibodies (9D10, Developmental

Studies Hybridoma Banke, University of Iowa) were used to distinguish only the CMs (green in Fig. 4.5). Rhodamine-conjugated phalloidin (0.5 μg/ml) stained F-actin in both the CMs and mFBs(red in Fig. 4.5). Because the titin staining designated only the cardiomyocytes, and F-actin staining designated all cell populations, the volume fraction of CMs was estimated as (pixels corresponding to titin)/(total pixels) and mFBs as (pixels corresponding to F-actin - pixels corresponding to titin)/(total pixels) [3]. In cases where ratios of mFB to total cells were used, this was determined by taking the volume fraction of mFB/volume fraction of all of the cells. If error caused the ratio to be out of possible bounds (0 to 1), then the ratio was assumed to be equal to the closest bound. Images were obtained on a Zeiss LSM 510 scanning confocal microscope using a 10x objective.

Stacks of images were acquired in several locations throughout the tissue and analyzed for volume fractions. Distribution of CMs and mFBs varied throughout the tissue, and led to wide variation of results at each data point (Fig. 4.5A-B). Figure 4.5A conveys the variation within a single stack in the middle of an EHT with orthogonal projections in both length and width slices. Projections show variance within stacks, and more specifically show cells concentrated on the surface with less dense concentrations in the center. Additionally, there was large variation of cell concentrations and types across the width of the tissue, as shown in the tile images in Figure 4.5B.

Techniques for determining the threshold to convert images to binary data was developed in the lab. Briefly, the threshold was estimated as the maximum curvature for the histogram of an individual image. The result was dependent on the brightness of the images and on the density of the cells. Pixels were summed to estimate area fractions in each image, and averages were taken throughout the depth of the tissue to obtain a volume fraction. Stacks were taken with 2 μm resolution along the optical axis into the depth of the tissue.

The initial volume fraction of all cells was estimated to be less than 5% of total volume, and the volume fraction of mFBs was estimated to be less than a few percent. These estimates assumed an initial total volume of 1 mL with cells as round spheres with diameters of approximately 25 μm. This made determining these absolute volume fraction values with accuracy extremely difficult. Additionally, these tissues were meant to be studied as fibrotic myocardium, and as such, eventually became dense and stiff at later stages of development. The primary and secondary titin antibodies, in some cases, had difficulty diffusing through the ECM to penetrate the interior cells. It is also important to note that volume fraction results were heavily dependent on brightness of both the red and green channels. When imaging, channels were kept as similar in brightness as possible. While taking stacks into the depth of the tissue, the ECM absorbed and reflected light in a nonlinear manner into the depth of the tissue, and the change in the brightness of the two channels was not necessarily the same. This could have caused inconsistencies between the green (titin) and red (F-actin) pixels as well.

4.3 Results

For the compared two sets of EHT, control and mFB enhanced, conduction velocities were estimated for several time points during development. A separate tissue with the same development conditions was fixed and stained for estimation of the mFB and CM volume fraction for that data point. Figure 4.6 shows the volume fraction of the mFBs increased with time for both the control and the mFB enhanced specimens while volume fraction of CMs decreased slightly over time for each of the sample sets. Error bars shown are for the standard deviation within a single tissue, and hundreds of images were analyzed for each data point, leading to the large variation.

Conduction velocities decreased with increased mFB concentration (volume of mFBs/total cells) in both the control and the mFB enhanced conditions(Fig. 4.7). Control EHT was tested on days 6, 8, and 17, while the mFB enhanced specimens were testing on days 5 and 7. The mFB enhanced tissues decreased in conduction velocity earlier than the control specimens (conduction velocity of less than 3 cm/sec by day 7). On day 17 for the control EHT, with an approximate mFB to total cell ratio of 0.45, there was no detectible calcium transient, and therefore was considered to have 0 conduction velocity. Y-axis error bars were calculated for the standard deviation for the measured conduction velocity in locations throughout a single specimen, while x-axis error bars were calculated for the standard error of the mean distribution of the ratio between mFBs and total cells volumes throughout a single tissue. Two-point anisotropic bounds, described in Chapter 3, were calculated for comparison by assuming the maximum conduction velocity corresponded to the two-point upper bound(Fig. 4.8). These bounds gave further context to the experimental trends.

4.4 Discussion

Conduction velocities were estimated for EHT, and compared to volume fraction data. The estimated volume fraction(Fig. 4.6) data showed that, as expected, initial mFB volume fraction was very low, but increased over time for both sample sets. mFBs proliferated and by day 17 had a volume fraction of over 0.1, but CM volume fraction showed a slight decrease over time. There are several possible explanations for this decrease. Cells may have been dying off to reach an optimum concentration, or they may have been dying off due to the starvation from nutrients with the constriction from remodeling. It is also possible that the number of cells did not change, but they compacted into myofibrils and decreased in total volume. Another important aspect is throughout time EHT remodels and compacts and thus changes in total volume, effecting these values as well.

Both in the various locations throughout the tissue, and even within a single stack there was a large variance of the concentrations of mFB and CMs. This initial estimate was sufficient for correlation with overall estimated conduction velocity for whole tissue measurements, but further studies are needed to determine more detailed volume fraction information. These volume fractions were estimated by imaging several stacks of images in different locations throughout the tissue, and then converting these into binary images in order to sum the pixels. Estimated volume fractions were determined by averaging these areas throughout the depth and in various locations of the tissue, but large variation due to differences in local cell concentrations made accurate volume fraction values difficult.

Another important parameter studied was the ratio of mFBs to total number of cells. Absolute volume fraction was very small in these tissues and difficult to measure exactly, but using the ratio of cell types was another measure of mFB concentration. Here it was used as insight into how mFB concentration affects entire specimen conduction velocity. Figure 4.7 conveys a decrease in conduction velocity with increase in this concentration of mFBs. A control tissue was testing on day 17 after twitching completely stopped. No calcium transient was detectable in this case, and so the conduction was assumed to be 0. This point at which conduction failed had a mFB/total cell volume ratio of approximately 0.45. When compared to the two-point anisotropic bounds from chapter 3, conduction velocity results followed the upper bounds until conduction failed on day 17 and then dropped to the lower bounds, similar to the electrophysiologic simulations from chapter 3.

These studies were coarse and planned future work will expand on these promising initial results. Improving volume fraction estimates would allow for more direct comparison of experimental data to theory. Possible future improvements include histological slicing to improve staining, and using fluorescent beads for calibrating channel brightness and binary image thresholding. Additionally, while these coarse estimates of conduction velocity give insight into the effect of mFBs on EHT, entire specimen optical mapping would be ideal. The level of detail obtained here makes it difficult to compare directly to a computational simulation results from chapter 3. Optical mapping would yield a higher level of detail for correlation with volume fraction data.

4.5 Conclusions

EHT, developed from embryonic cardiomyocytes and fibroblasts as an experimental model, was studied over time for two sets of specimens, control and mFB-enriched. Volume fraction and conduction velocities were estimated over 3 days for the control and 2 days for the mFB enriched tissues to better understand the effects of mFBs on electrical function of EHT. In both cases, mFB absolute volume fraction increased over the time period, most likely from proliferation, while CM absolute volume fraction decreased. This decrease could be attributed to cell death or cells being compacting into myofibrils. As a measure of mFB concentration, the ratio of mFB/total cell volume was studied for each data point as well. Conduction velocity of groups of cells throughout the tissue were estimated using calcium transient imaging. Conduction velocity was maximum, averaging 6 cm/second for the control tissue on day 6, with a mFB/total cell volume ratio of about 0.1. The mFB enriched tissue tested on day 5 was estimated to have a lower conduction velocity of about 4 cm/second with a mFB/total cell volume ratio of about 0.12. In general, conduction velocity decreased with mFB concentration until failing on day 17 with a mFB/total cell volume of about 0.45. While these preliminary coarse results are promising and indicate a strong effect of mFB concentration on conduction velocity in EHT, several limitations exist. In future work, more accurate volume fraction data is necessary for correlation with theory and computational models. Additionally, this low resolution method for estimating conduction velocity should be expanding to obtain more detail. Ideally this would be done by entire specimen optical mapping to acquire a sufficient level of detail.

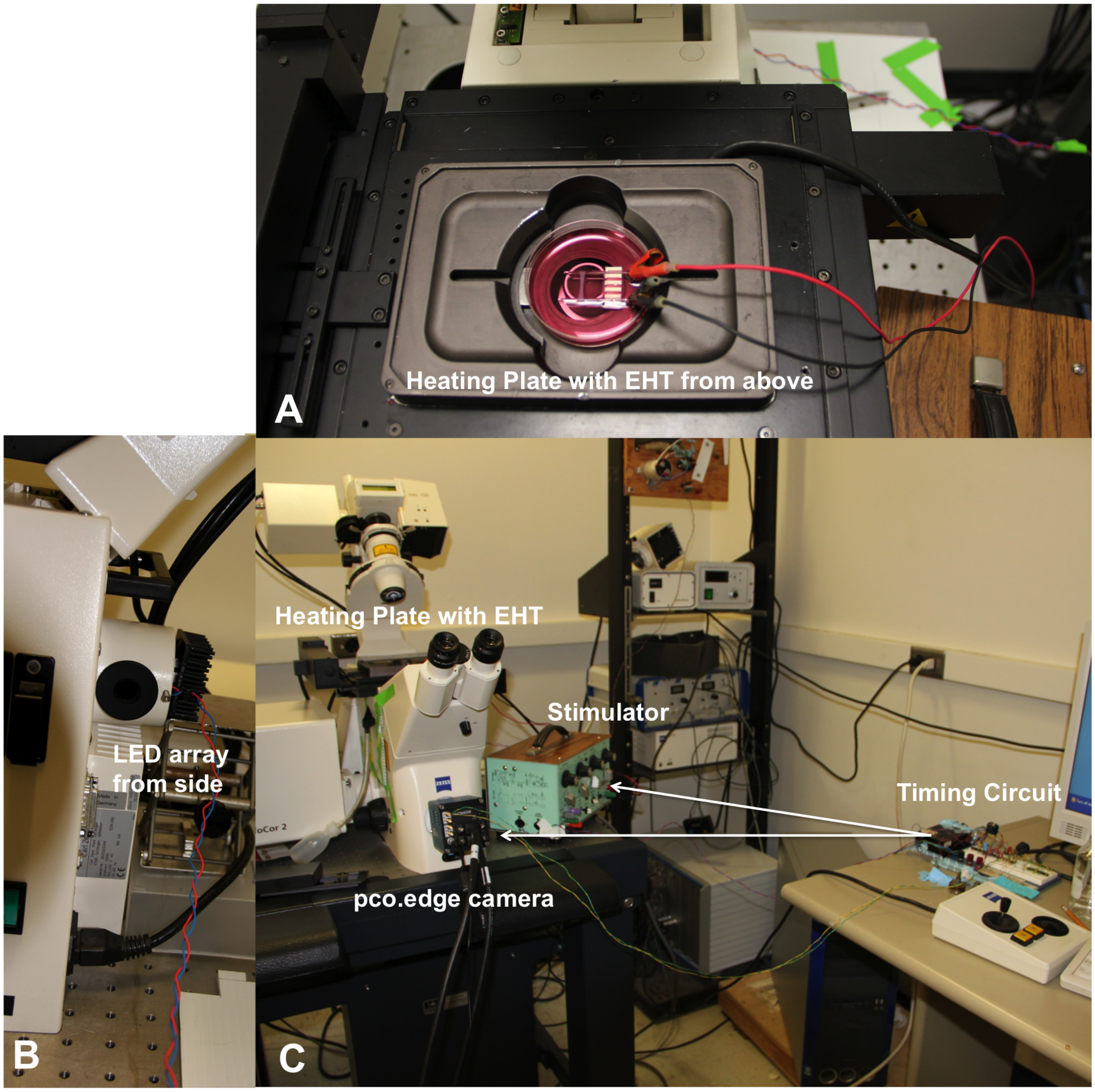

Figure 4.2: Experimental setup
EHT was stimulated in sync with the camera being triggered to acquire data in order to obtain the calcium transient in a small area of the tissue from the time of stimulation. Illumination was produced by an LED array in place of a lamp on a Zeiss microscope using a 10x objective. A pco.edge camera was used to acquire the videos at about 120 frames/second.

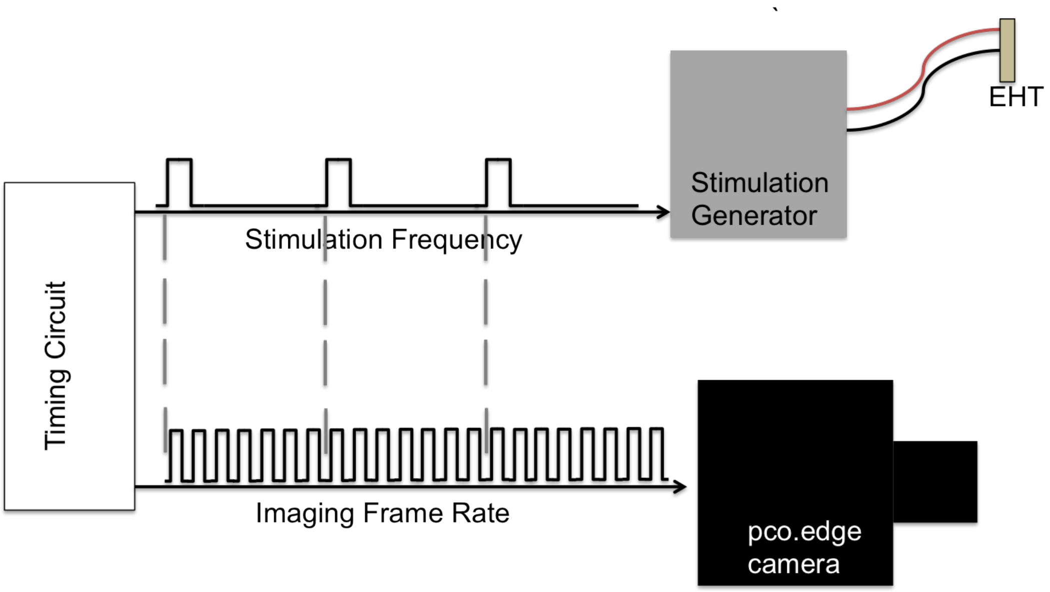

Figure 4.3: Timing circuit schematic
The timing circuit schematic shows the stimulation of the tissue occurring in sync with the triggering of the camera to record. This allowed for the acquisition of the fluorescence intensity from the time of EHT stimulation.

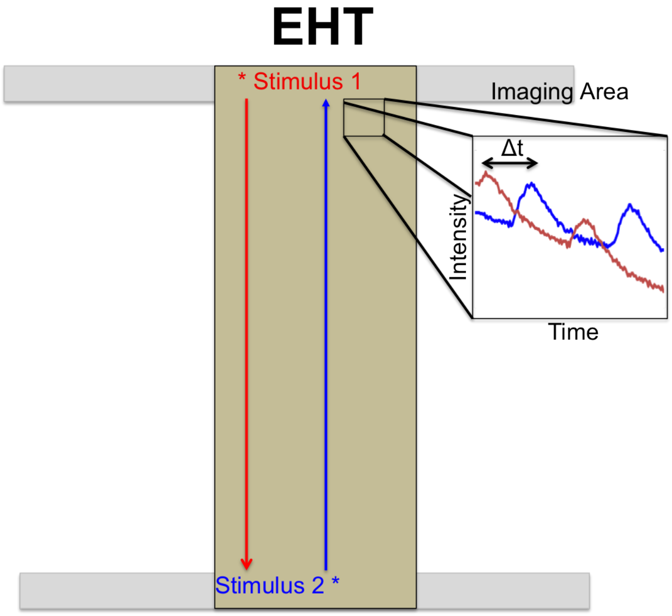

Figure 4.4: Estimation of conduction velocity
EHT were stimulated near a small area while imaging, and then stimulated from the opposite end while imaging the same area. Comparing the two calcium transients, yields Δt between the two peaks of the calcium transient. This was then the time elapsed while the impulse traveled across the length of the tissue and was used to estimate the conduction velocity of the tissue.

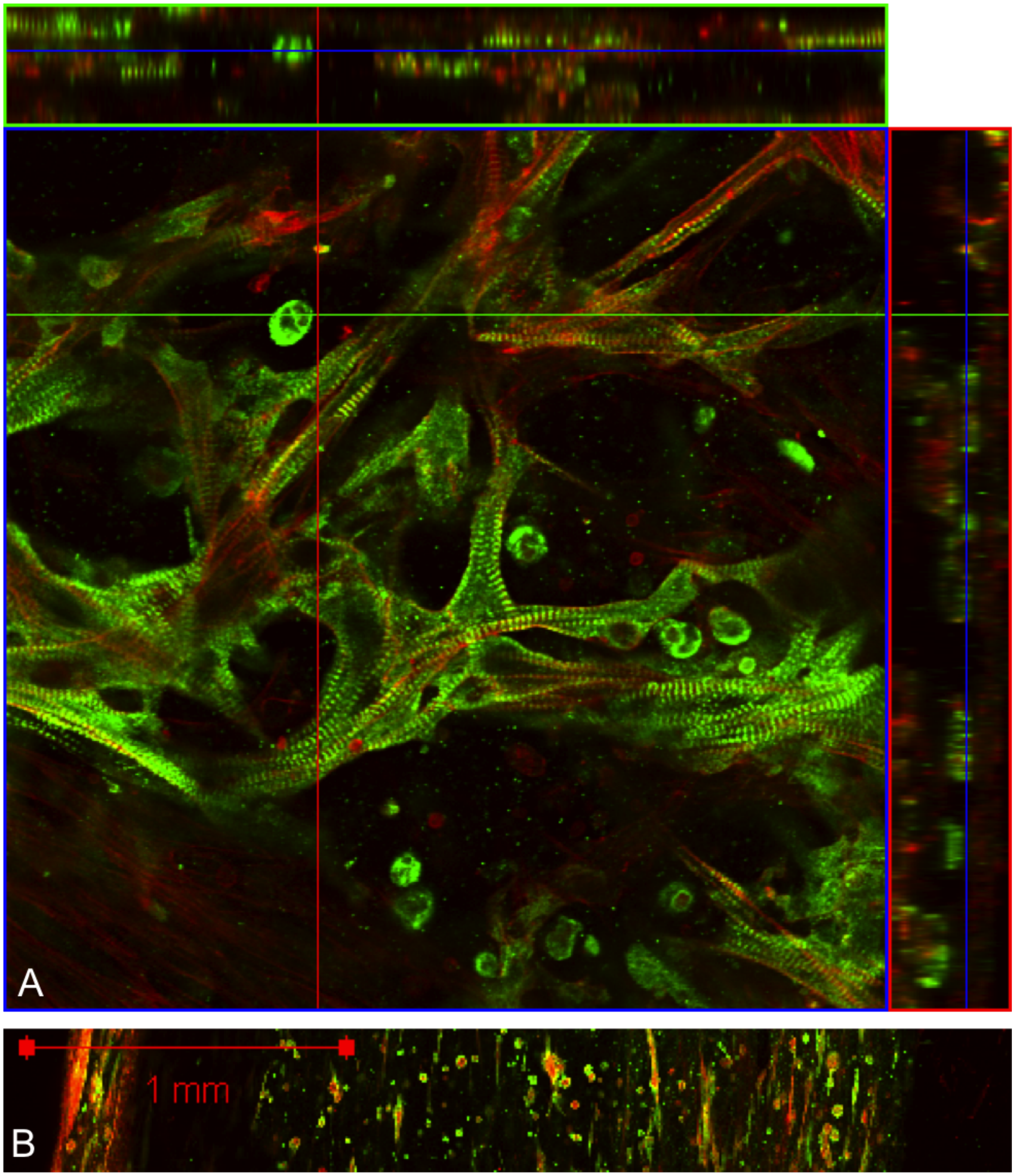

Figure 4.5: Immunofluorescence volume fraction estimation
A. A representative immunofluorescence image is shown with orthogonal view sliced from left to right (shown in top picture) and top to bottom (shown in picture to right). Example picture shows CMs stained for titin (green) and all cells stained for F-actin (red) B. A tile scan across entire tissue conveys the large variation in cell density and cell type throughout the tissue.

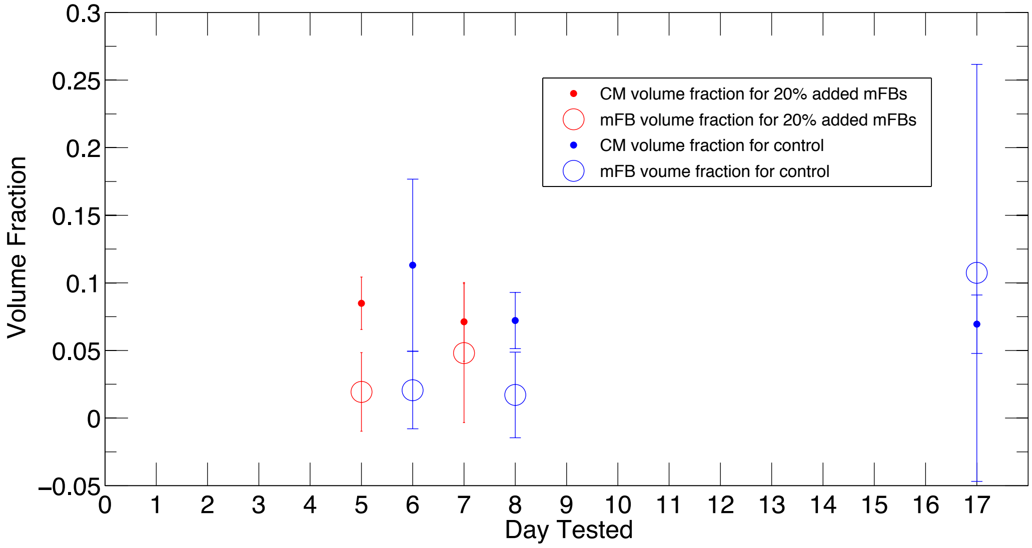

Figure 4.6: Volume fraction of CMs and mFBs tested over time
Volume fraction of CMs and mFBs were tested over time and shown here with error bars of standard deviation determined by the variance within a single sample. Hundreds of images were taken in each sample, leading to a large variation in results. Red points correspond to mFB-enhanced EHT while blue points correspond to the control tissue.

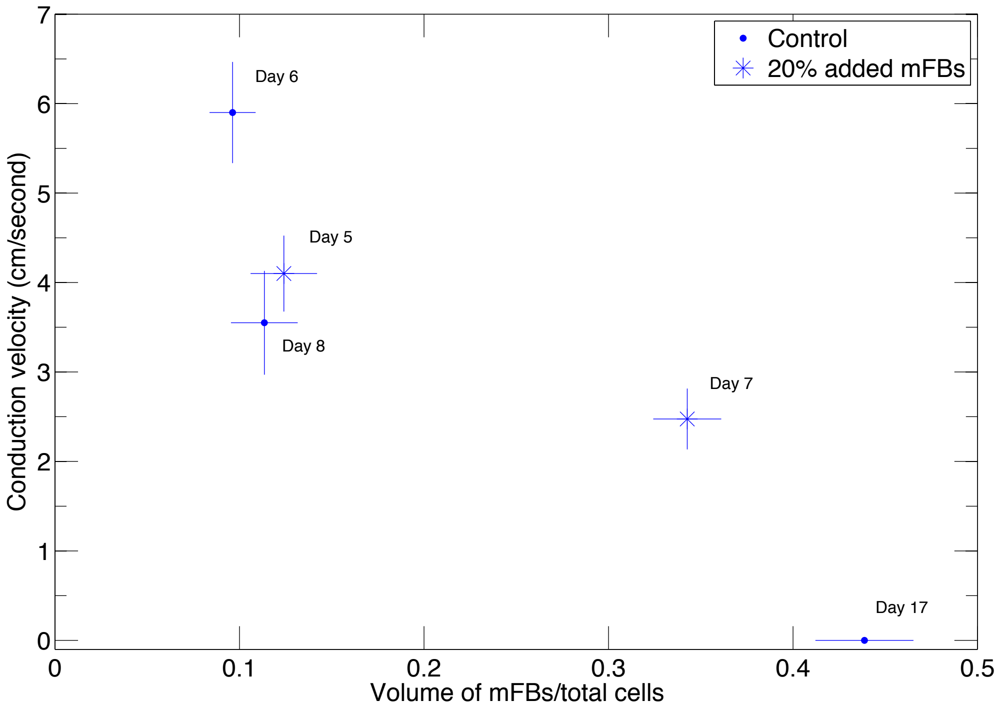

Figure 4.7: Estimated conduction velocities for increasing mFB volume fractions Conduction velocities in EHT was studied for increasing mFB volume fractions. A single control EHT was tested per day on 6, 8, and 17, while the mFB enhanced specimens were testing on days 5 and 7. The mFB enhanced tissues decreased in conduction velocity earlier than the control specimens. Error bars were determined by standard deviation on the y-axis and standard error of the mean on the x-axis. Only one EHT was tested for each data point and conduction velocity standard deviation was for variation within a single specimen.

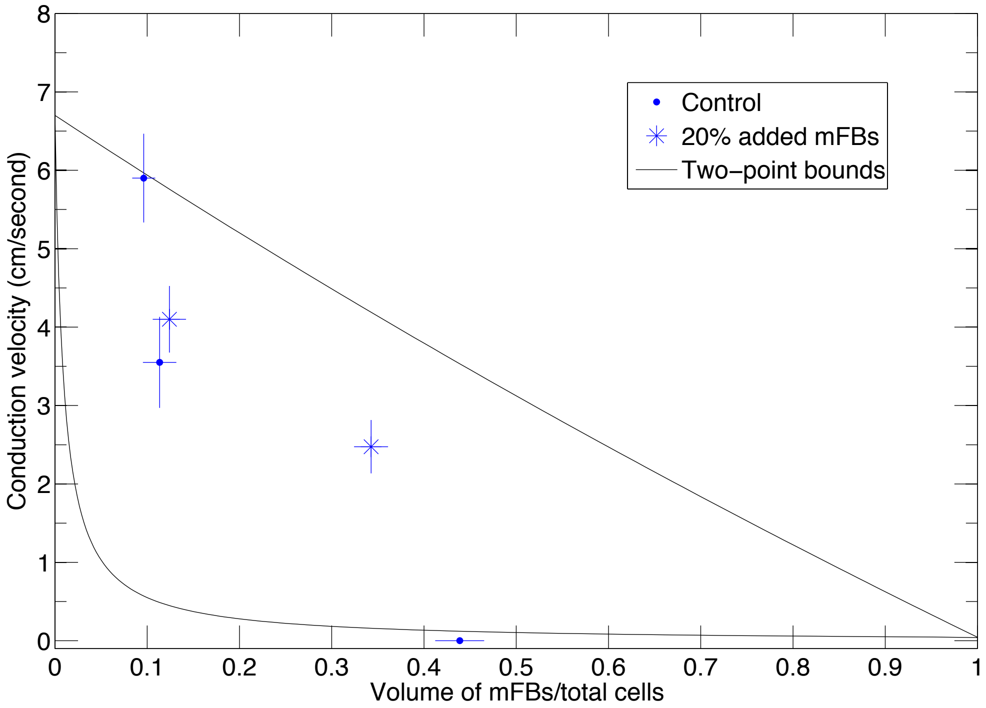

Figure 4.8: Estimated conduction velocities compared to two-point bounds Estimated conduction velocities, compared to two-point bounds from Chapter 3, followed within the bounds until failing conduction.

Chapter 5

Two-dimensional electromechanical coupled simulations

5.1 Introduction

In response to certain pathologies, such as hypertension or infarction, the body responds by converting fibroblasts to myofibroblasts(mFBs) to preserve the overall function of the heart. mFBs are larger and more contractile than fibroblasts, but retain their capacity to secrete collagen. While important in healing, these cells can alter the mechanical compliance and electrical functioning of the heart, ultimately causing mechanical function degradation as well as electrical function conditions such as arrhythmias.

It is not well understood if simply preventing the formation of myofibroblasts or abolishing their effects in the heart would be suitable since some level of mFBs function is adaptive. In developing therapeutic approaches it is therefore essential to understand how myofibroblasts interact with cardiomyocytes to modulate the electromechanical functions of the heart, and how changes in mFBs function, e.g., attenuation of mFBs contractility or partial elimination of interstitial myofibroblasts, would affect these functions.

Here computational and experimental models of heart muscle with defined fractions of myofibroblasts were developed to explore this problem. The experimental model consists of engineered heart tissue (EHT) assembled from embryonic cardiomyocytes (CMs) and containing defined fractions of mFBs randomly distributed. EHT has been shown by us and others to replicate many features of the biophysics of natural myocardium [42, 7, 3]. Data from our experimental model suggested that a range of concentrations of myofibroblasts promote periodic contraction of EHT, while higher concentrations obstruct this.

The goal of this work was to focus on a well-defined system, and look at effects of individual cells on the mechanical functioning of myocardium. Continuum models, such as those by Hunter et al. and Vigmond et al., must assume certain parameters, and focus on the macroscopic myocardium functioning [12, 33]. The main focus here was to use a discrete approach to understand from the cellular level how mFBs and CMs interact with the goal being to find relationships between cell volume fraction and overall contractile function.

This work extends previous work from Chapter 3 by coupling the Luo-Rudy Dynamic CM model electrophysiologic simulation results to an excitation-contraction model and finally to an overall tissue mechanics model where CMs and mFBs lie in a sheet attached in parallel to the extracellular matrix (ECM). In small concentrations, mFBs are used to adapt and stabilize tissue, and have little negative effect on overall tissue electrical or mechanical functioning. Results show that a mechanical critical point (where mechanical functioning starts to degrade significantly) occurs at a slightly lower volume fraction of mFBs (about 0.22) than electrical percolation occurs from Chapter 3.

5.2 Methods

5.2.1 Experimental

EHT preparation

EHT specimens were prepared as described previously [7] by isolating cardiomyocytes from 10-day-old chicken embryos, and suspending the cells (approximately 1.4 million/ml, final concentration) in Type I rat tail collagen, DMEM with 10% FBS, and 4% chicken embryo extract. The mixture was poured into an 8-well plate and placed in a 37°C CO_2 incubator producing a loose collagen gels in which cells were randomly distributed. Within 4 days the cardiomyocytes began contracting independently and experiments were conducted.

Because the fibroblasts adhere more strongly than the CMs to plastic cell culture dishes, they were separated by allowing the primary cell suspension to rest in a culture dish for a defined time period (1 hour and 10 minutes). CMs were then replaced with mFBs to vary ratios from near 0% to 30% for comparison in mechanical force testing.

Mechanical force data

Mechanical force testing was preformed daily once EHT began to spontaneously and synchronously contract 4 days after preparation. Data was acquired using a robotically controlled probe and force transducer system (Palpator, InvivoSciences, LLC)(Fig. 5.1). Specimens in an 8-well plate were each pre-conditioned 3 times to 15% strain, followed by 30 minutes of relaxation. Specimens were then stretched to 15% strain while resulting forces were monitored. Baseline and twitch forces were visible in resulting data. Where baseline force was considered the steady state static force (minimum force), and the twitch force was the difference between the maximum cyclic force and the baseline force.

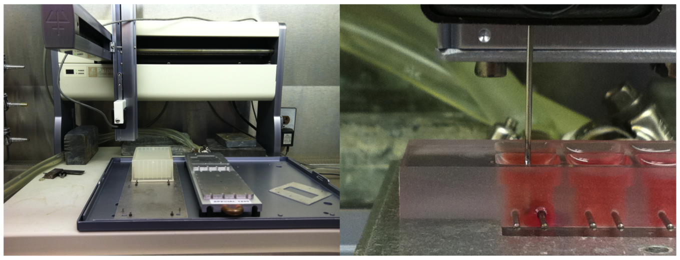

Figure 5.1: Mechanical force testing equipment
Mechanical force testing equipment (Palpator, InvivoSciences, LLC). A roboticaly controlled probe stretched tissue while monitoring resulting forces.

5.2.2 Immunofluorescence volume fraction analysis for CMs and mFBs in EHTs

Specimens from days 4, 5, 6, 7, and 17 were fixed using 4% paraformaldehyde to determine volume fractions of CMs and mFBs. Imaging methods and analysis techniques were described in Chapter 4. Briefly, for titin labeling, specific monoclonal antibodies (9D10, Developmental Studies Hybridoma Bank, University of Iowa) were used to distinguish only the CMs (green in Fig. 4.5). Rhodamine-conjugated phalloidin (0.5 μg/ml) stained F-actin in both the CMs and mFBs(red in Fig. 4.5). Because the titin staining designated only the cardiomyocytes, and F-actin staining designated all cell populations, the volume fraction of CMs was estimated as (pixels corresponding to titin)/(total pixels) and mFBs as (pixels corresponding to F-actin - pixels corresponding to titin)/(total pixels) [3]. Images were obtained on a Zeiss LSM 510 scanning confocal microscope using a 10x objective.

Stacks of images were acquired in several locations throughout the tissue and area fractions of each were averaged to obtain volume fraction estimates. Distribution of CMs and mFBs varied throughout the tissue, and led to wide variation of volume fractions at each data point (Chapter 4). Techniques for determining the threshold to convert these images to binary data were developed in the lab. The threshold was estimated to occur at the maximum curvature of the histogram in an individual image. The result was significantly dependent on the brightness of the images and on the density of the cells. The initial volume of all cells was estimated to be less than 5% of total volume, and the volume of mFBs was estimated to be less than a few percent (Chapter 4). This made determining these values with accuracy extremely difficult. Because volume fraction was not determined for all time points due to limitations in numbers of specimens, as an estimate, data acquired from the endpoints was interpolated for the remaining points. This estimate was thought to be sufficient in comparing trends between the experimental data and the computational model results.

5.2.3 Computational

These studies expanded on previous work (Chapter 3) of electrophysiologic simulation results (CM ionic model of Luo-Rudy Dynamic) by coupling with two more classes of models, an excitation contraction model of Nickerson et al. [24] for individual CMs, and the overall tissue mechanics from several existing models. The goal was to study the combined mechanical and electrical effects of mFBs on the functioning of EHT specimens. The mechanical model combined several modified existing models of cells within an ECM.

Excitation-contraction modeling at the level of individual CMs

Many detailed excitation-contraction models exist with varying degrees of detail [32]. For a general understanding of the combined electrical and mechanical effects of mFBs, predicted patterns of depolarization from previous electrophysiologic studies (Chapter 3) were related to tissue level contractile force, through the model of Nickerson et al. [24] was implemented which builds from the Hunter-McCulloch ter Keurs model [12] to predict CM contractile stress $T([Ca^{2+}]_i, \lambda, t)$ as a function of time t, the concentration $[Ca^{2+}]_i$ of free myoplasmic Ca^{2+}, and the cellular stretch rate λ and its time history; the model can be inverted to predict $\lambda(T, [Ca^{2+}]_i, t)$ given the entire loading history of the cell from $-\infty$ to t. The internal workings of the model involve three state variables: the concentration $[Ca^{2+}]_b$ of Ca^{2+} bound to troponin C, the fraction z of actin binding sites that are occupied by actomyosin crossbridges, and the state-dependent maximum activation stress To. The internal workings begin with a binding kinetics equation for $[Ca^{2+}]_b$, which depends on the current contractile stress T:

$$\frac{d[Ca_b^{2+}]}{dt} = \rho_0[Ca^{2+}]_i([Ca^{2+}]_{b,max} - [Ca^{2+}]_b) - \rho_1(1 - \frac{T}{\gamma T_0})[Ca^{2+}]_b, \tag{5.1}$$

$[Ca^{2+}]_b$ determines the rate of change of z:

$$\frac{dz}{dt} = \alpha_0 \left(\left(\frac{[Ca^{2+}]_b}{C_{50}} \right)^n (1 - z) - 1 \right), \tag{5.2}$$

where α_0 is a constant and n and $log_{10}(C_{50})$ increase linearly with the degree of stretch λ [12]. The maximum activation stress scales with stretch and with increasing numbers of cross-bridges:

$$T_0 = T_{ref}\left(1 + \beta_0(\lambda - 1)\right) z \tag{5.3}$$

Finally, the Bergel-Hunter fading memory model [11] is applied to account for the observation that following a step shortening, the cells recover lost tension actively over three distinct timescales:

$$T = T_0 \frac{1 + aQ}{1 - Q}, Q = \sum_{i=1}^{3} A_i \int_{-\infty}^{t} e^{-\alpha_i (t-\tau)\frac{d\lambda}{dt}\tau} d\tau \tag{5.4}$$

constants for these equations have been fit by Hunter et al. [12] for rat trabeculae, and can be found in detail in Appendix B. Note that Q is most important following rapid length changes. Parameters for this mechanical model have not been calibrated for chick embryo cells. Mammalian values were used with the aim of obtaining qualitative comparison between simulation and experiment for EHTs with chick embryo cells.

Cell Models

EHT was modeled by combining several modified existing models of CMs and mFBs in parallel with ECM in a sheet with randomly distributed patterns following the results from Chapter 3 (Figure 3.1).

Extracellular matrix was modeled as a standard linear solid, (Fig. 5.2) using previously published data for material properties, [3, 40] where k^s_{ECM} was the series ECM stiffness, k^p_{ECM} was the parallel ECM stiffness, and η_{ECM} was the ECM viscosity.

$$\frac{d\epsilon(t)}{dt} = (k^p_{ECM} + k^s_{ECM})^{-1} \cdot \left[\frac{d\sigma(t)}{dt}\frac{k^s_{ECM}}{\eta}\sigma(t) - \frac{k^s_{ECM}k^p_{ECM}}{\eta_{ECM}}\epsilon(t)\right]. \tag{5.5}$$

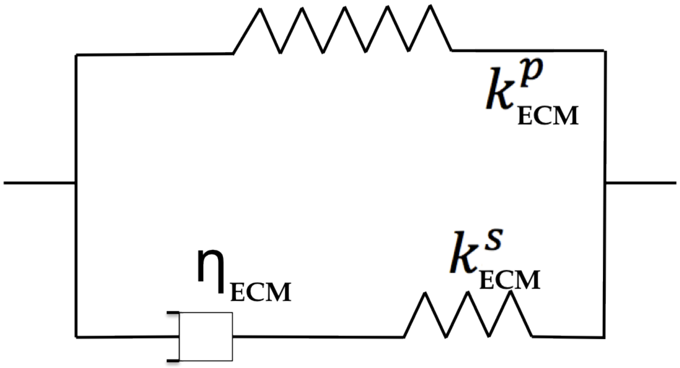

Figure 5.2: ECM model schematic
ECM was modeled as a standard linear solid using previously published material properties for parameters.

Cardiomyocytes were modeled as modified Hill elements with an active, dynamic element that produced a dynamic stress $F(t)$, a passive parallel element of stiffness k^p, a series stiffness k^s, and a viscosity η (Figure 5.3) [3, 36] . The parallel stiffness represented the inherent compliance of the contractile assembly of a cell. The series stiffness represented compliance such as that associated with titin that transmits forces to the ends of the specimen [36]. Although earlier work showed that cells of many types exhibit nonlinear elasticity [40, 34], this linear viscoelastic model of passive cell mechanics was a first order approximation that is valid strictly only in the sense of incremental behavior [25]. Parameters used were previously published for EHT and can be found in detail in Appendix B [3].

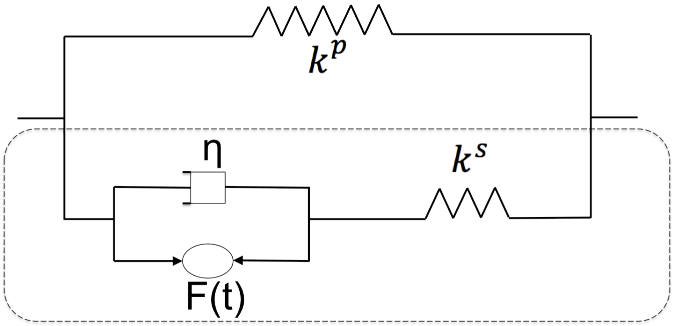

Figure 5.3: Cells model schematic
Cells were modeled as modified hill elements where CMs contained a dynamic contractile force determined by the HMT model and mFBs contained a static contractile force. All parameters were determined using previously published data in the lab. Cells were then added in parallel to the ECM.

Myofibroblasts were modeled following Zahalak [40] as modified Hill elements. These elements differed from the cardiomyocyte elements in that the dynamic twitch stress was replaced by a steady, static contractile stress, and their mechanical parameters followed those previously published for fibroblast cells [40].

Finite Element Methods

This two-dimensional overall tissue mechanics model was developed in the commercial software package COMSOL Multiphysics using the viscoelastic definition to describe the ECM material. The model was coupled through MatLab to incorporate the individual cell contraction from small subsections of the previous electrophysiologic simulations (Chapter 3). Cell parallel stiffness (k^p) was added to the ECM parallel stiffness within the viscoelastic model, and the remaining cell contraction branch (dashed line in Fig. 5.3) was solved using the Partial Differential Equation internal COMSOL module(Eq. 5.6). Finally, these results were integrated by calibrating them as individual thermal stresses in each corresponding cell to complete the model. Thermal stresses were calibrated with the thermal expansion coefficient and material properties to add the corresponding stress in parallel with the ECM at the individual cell level. Because of the intense computational nature of the simulations, small subsections were taken from the original large volume electrophysiologic simulations to obtain approximate overall tissue mechanics.

$$\frac{d\epsilon(t)}{dt} = \frac{1}{k^s}\frac{d\sigma(t)}{dt} + \frac{\sigma - F(t)}{\eta} \tag{5.6}$$

5.3 Results

Experimental and computational models were used to explore the effects of mFBs on overall EHT electromechanical functioning. Mechanical force data of specimens with varying concentrations of mFBs was acquired over time beginning 4 days after preparation, when tissues began to twitch synchronously, and until day 17, when twitch force had significantly decayed. Tissues remodeled and contracted over time while cells proliferated and died off from their original concentrations (Fig. 5.4). During this development, in general, mechanical twitch force of specimens increased until reaching a peak, and then slowly decreased(Fig. 5.5). Twitch and baseline forces for the mechanical force testing (as well as simulation results) were measured by following the convention shown in Figure 5.6.

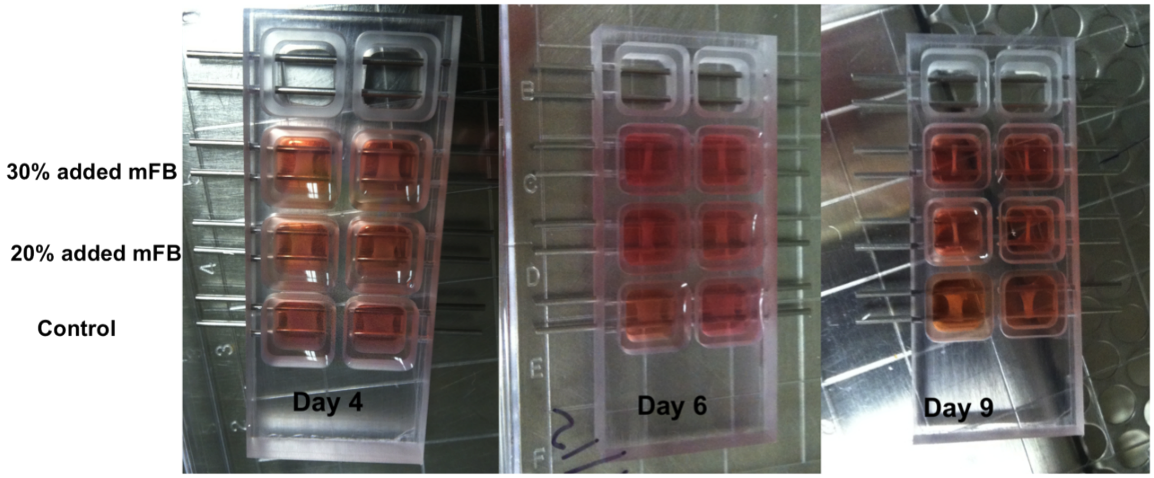

Figure 5.4: EHT remodeling over time
Tissue specimens with varying ratios of mFBs corresponding to 4, 6, and 9 days after preparation. EHTs in early stages were not very remodeled, but by day 17 tissues were significantly more remodeled.

During critical time points, specimen samples were fixed and stained to estimate the volume fractions of CMs and mFBs. Determining an absolute volume fraction of CMs and mFBs was difficult because initial concentrations were so small. An estimate of initial volume of total cells was approximately 5%, and of mFBs was less than a few percent of total volume. Even though tissues began to contract by day 4, it was difficult to determine exact volume fractions of cells in these low concentrations. Similar to results shown in Chapter 4, estimates show qualitatively that mFBs volume fraction increased over time, while CM volume fraction decreased over time(Fig. 5.7). Estimated mFB volume fraction corresponded to mechanical force data from Figure 5.5. Average twitch force for each initial concentration at each time point was compared to the corresponding estimated mFB volume fraction(Fig. 5.8).

These experimental results were the basis for the two-dimensional electromechanical model. Overall tissue mechanics were studies for two cases while varying mFB volume fraction from 0 to 1(Fig. 5.9). In the first case, even when conduction failed

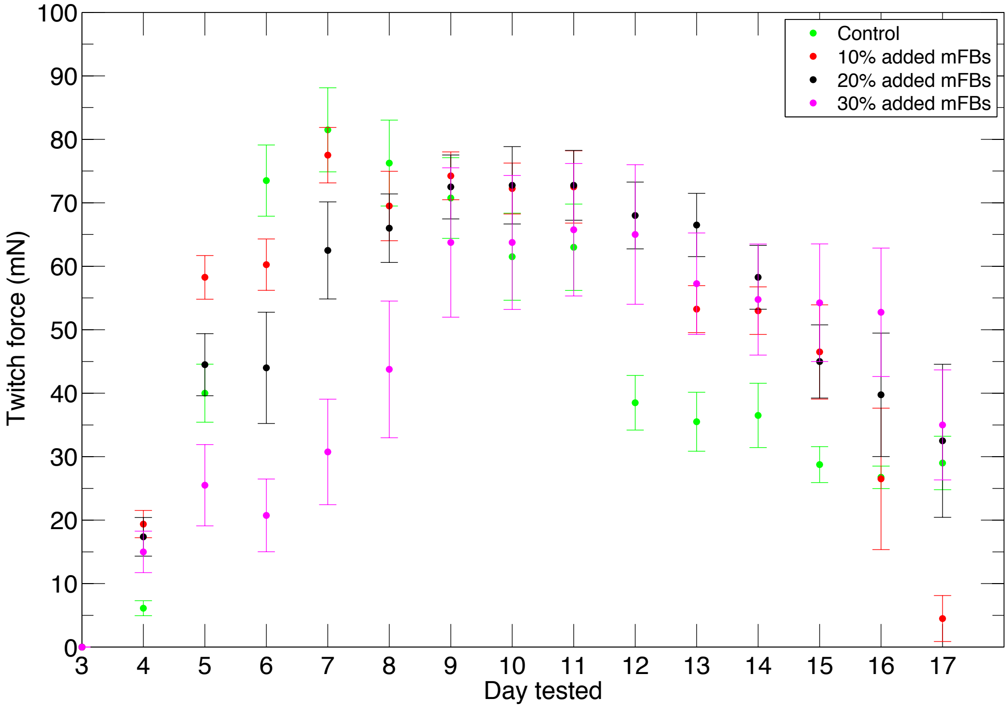

Figure 5.5: Evolution of twitch force over time
The evolution of twitch force was acquired over time with various initial mFB concentrations, for 8 specimens at each data point. Standard deviation was determined for these specimens to yield the shown error bars.

in corresponding electrophysiologic simulation, it was assumed that no electrical percolation had occurred. A subsection of cells was chosen from before the conduction block in the simulation, and thus, depolarized and contracted, contributing to the overall mechanics (blue). For comparison and to delineate electrical and mechanical effects, the second study used results from a subsection of cells located after the conduction block, and thus had no CM contraction (red). Results were equivalent until the electrical percolation (about 0.28 mFB volume fraction) caused failed conduction and CMs no longer contracted.

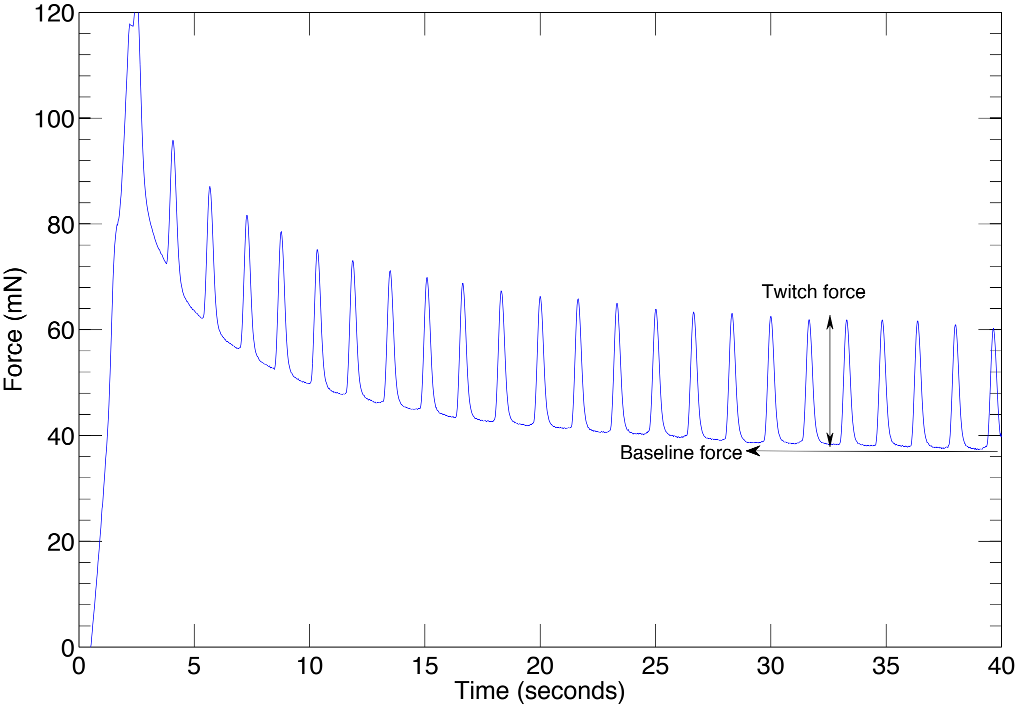

Figure 5.6: Baseline and twitch force convention
The convention used for quantification of raw mechanical force data and simulation results was that the steady state minimum force was considered baseline force, while the twitch force was considered the difference between the maximum and minimum steady steady forces as shown.

5.4 Discussion

Data from our experimental model suggested that a range of concentrations of myofibroblasts promote periodic contraction of EHT, while higher concentrations obstruct this(Fig. 5.5). Data was acquired for EHT with various initial mFB concentrations from 0% to 30% for days 4 to 17 after being prepared. Specimens with higher initial mFB concentrations initially had larger average twitch force until day 6 when the control specimen was highest. The maximum average twitch force detected was about 80 mN on day 7 from the control tissue. After day 9 there was not a significant difference between specimens with different initial concentrations.

As was discussed in Chapter 4, volume fractions for CMs and mFBs were difficult to quantify because of their small absolute values (less than 5% of total volume). Using immunofluorescence and imaging techniques described in chapter 4, estimates were made for specimens at critical time points(Fig. 5.7). For all concentrations, there was not a significant difference in measured volume fraction of mFBs or CMs over days 4-7. We are unsure if there was simply no significant change because there was little remodeling, or if the change was not measurable using these methods. mFB volume was very low (a few percent), and CM volume fraction was slightly greater than 10% for all initial concentrations. Volume fraction accuracy was not precise enough to determine significant differences in volume fractions during the beginning stages of development. Variation of cell distribution from location to location and within a stack caused large variations in volume fractions measured in different images, and therefore large standard deviations, as was discussed in Chapter 4. By day 17, there was a measurable increase in mFB volume fraction and decrease in CM volume fraction for all initial concentrations.

The corresponding average twitch force measurements and volume fraction estimates were combined to yield further insight into general trends of the effects of mFBs on EHT functioning(Fig. 5.8). While tissues were begining to form, small concentrations of mFBs seemed to improve twitch force. Over certain concentrations, the forces plateaued, indicating mFB had no significant effect on overall functioning. Finally, average twitch force in all specimens began to decrease at higher mFB concentrations, supporting the hypothesis that mFBs eventually degrade overall tissue functioning.

To study this further, a two-dimensional electromechanical model was developed. The model expanded on electrophysiologic models in Chapter 3 by coupling subsections of cells from these results to an excitation-contraction model and an overall tissue model. Two sets of studies were used to delineate electrical effects and mechanical effects of mFBs on EHT. The first assumed that there was no electrical percolation, and so all CMs depolarized and contracted. These electrophysiology results were taken from cells located before the conduction was blocked in a simulation. The resulting baseline and twitch forces give insight into mechanical effects of mFBs(Fig. 5.9). Small concentrations of mFBs showed little effect on overall tissue mechanics until a critical volume fraction of about 0.22. Here twitch force began to decrease and baseline force began to increase. This trend continued until a mFB volume fraction of 1 where the twitch force was completely diminished. In comparison, another study used results from sections of cells located beyond a conduction block where CMs did not depolarize or contract. While results were the same initially, beyond the electrical percolation threshold of about 0.28, twitch force dropped to 0, and baseline force dropped slightly as well, indicating the CMs contraction played a role in steady state baseline force as well. Baseline force then continued to increase to ultimately match that of the original study when the volume fraction was 1.

Additionally, ECM stiffening due to increased mFB concentration was not considered in Figure 5.9, but results from Chapter 2 would suggest, if considered, the effect would be fairly linear, and the twitch force would rise somewhat before the precipitous drop. In general, results support the experimental results indicating that mFBs, in small concentrations, have little effect on overall tissue functioning, but at high concentrations can both degrade mechanical functioning and eventually completely block electrical conduction, causing seising of twitch force.

These studies were meant to be a high level study of the effects of mFBs on EHT, and as such, there are several improvements that can be made for future studies. First, better estimates of volume fractions of mFBs and CMs would allow for more direct comparison. This is difficult, as previously explained, because of the low absolute volume fractions of cells compared to the entire tissue. Also, a wide range of concentrations and variations throughout the tissue lead to large standard deviations. Finally in dense areas of EHT, the titin anitbody may not able to diffuse uniformly into all cells. Some improvements to determine a more accurate volume fraction include staining thin slices to assist in diffusion of antibodies to all cells, and using fluorescent beads for channel calibration and binary image thresholding to ensure consistency between images. Other options are to move away from this kind of image analysis and use cell sorting instead, but this would not yield the absolute volume fraction that we are most interested in. Future work is to obtain mechanical force data while preforming optical imaging (Chapter 4), allowing direct comparison of mechanical and electrical function of EHT. Other limitations for this mechanoelectric model include appropriate material properties. Values for the electrophysiologic model used from the Luo-Rudy Dynamic model were based on guinea pig ventricular cells, while the mechanical properties were based on data from embryonic chicken cells. As a qualitative comparison this was sufficient, but consistent cell type data would allow for a more direct comparison.

5.5 Conclusions

Mechanical force testing of experimental models indicated mFBs, in small concentrations, improve EHT functioning, but in higher concentrations, can lead to deleterious effects. The general trend of EHT mechanical force is similar for the various initial mFB concentrations. Initially the twitch force increased to a maximum where it plateaued, and eventually decreased slowly until it stopped completely. In general, estimated mFB volume fraction increased over time, while CMs volume fraction decreased over time. Correlating the rough estimates for mFB volume fraction and average twitch force yielded some context to the effects of mFBs on EHT. The trend suggests that in certain concentrations, mFBs have little effect on overall tissue mechanics, but if mFBs proliferate, they can eventually cause the mechanical twitching to completely shut down. The two-dimensional electromechanical model gives further insight into these results. The model concentrated on two separate situations: those where mechanical contributors primarily caused deleterious effects and those where electrical contributors primarily caused deleterious effects. These two cases were the same up to the electrical percolation threshold discussed in Chapter 3. Results supported the experimental data, indicating, in small concentrations, mFB have little effect on mechanics, but as mFB concentration increases, at a critical mechanical point, contrary to our expectation from Chapter 2, twitch force begins to decrease, and finally at some electrical percolation threshold, EHT twitching completely stops due to electrical impulse failure. Improvements can be made to these studies, specifically in determining more accurate volume fraction data. However, results, when interpreted through the computational model, indicate that myofibroblasts can improve contractile function up to a volume fraction on the order of 25%. Thereafter, both mechanical and electrical effects lead to shut-down of contractile function. The competition between these is won by the electrophysiologic effects. However, this needs to be checked as further refined model parameters become available through future experimentation.

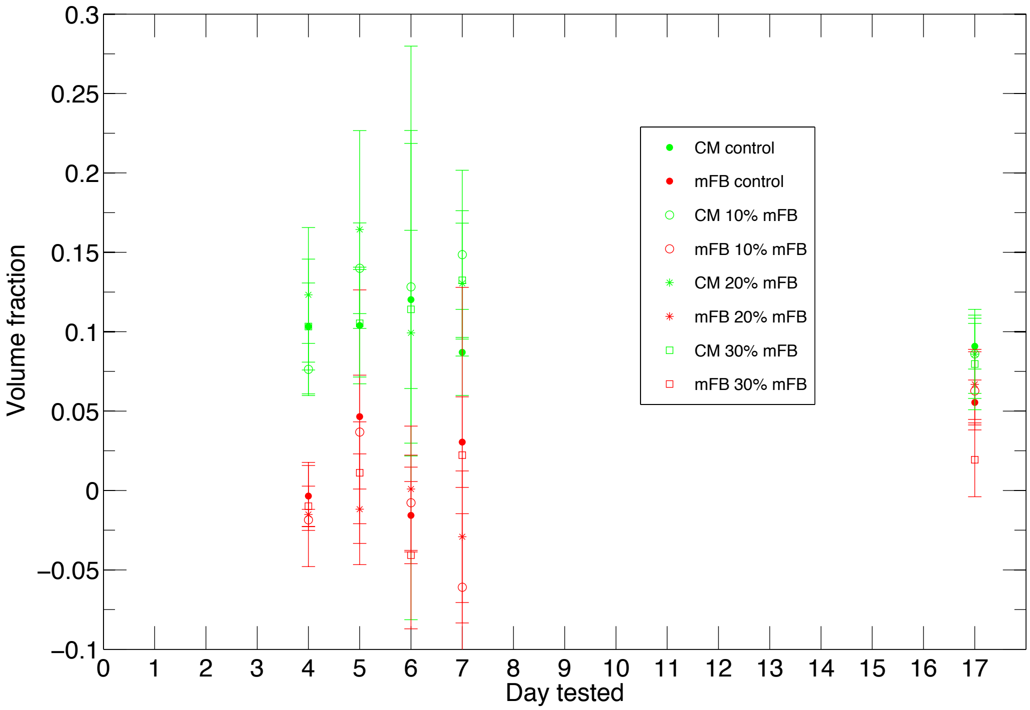

Figure 5.7: Evolution of volume fraction over time
The evolution of the volume fraction of CMs and mFBs were studied over time for EHT with varying initial concentrations of mFBs. A single sample was imaged to determine volume fraction for each data point, and the standard deviation was determined by the hundreds of images taken within a single specimen. No measurable change in volume fraction occurred for either the CMs or mFBs during days 4-7, but by day 17, the mFB volume fraction had increased, while the CM volume fraction had decreased slightly in all initial concentrations. Estimated volume fractions were much lower than expected due to what may be an underestimate due to imaging and analysis limitations.

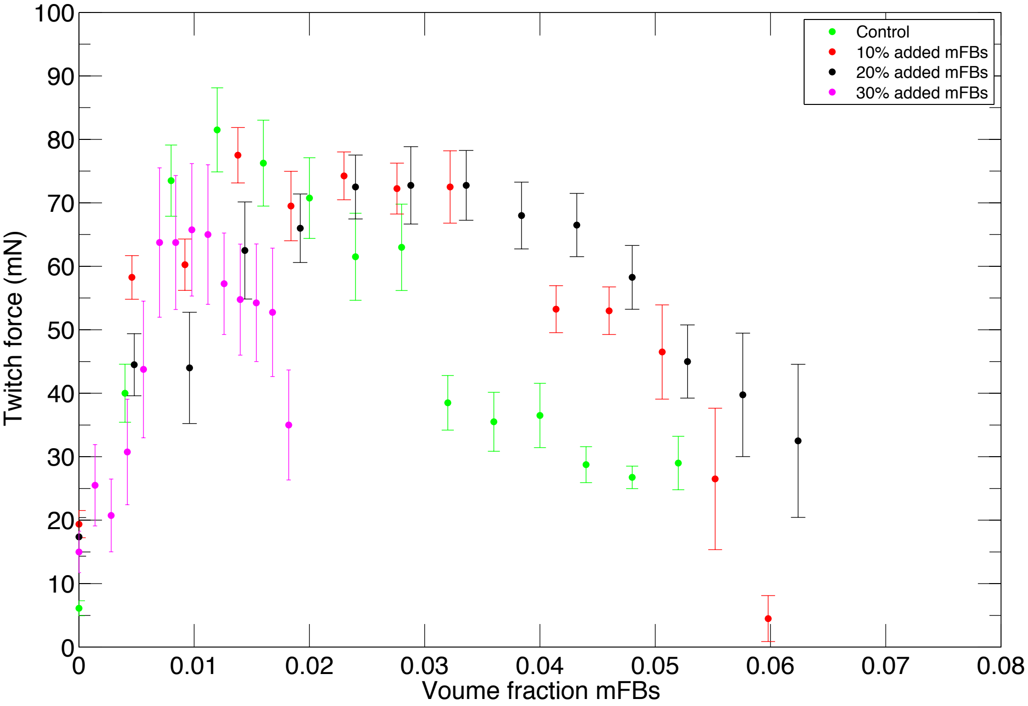

Figure 5.8: Twitch force compared to mFB volume fraction
The measured twitch forces were compared to the corresponding mFB volume fraction data, and data points without measured volume fractions were interpolated between the endpoints. As in the previous twitch force plot, error bars represent standard deviations of the 8 samples tested for each data point.

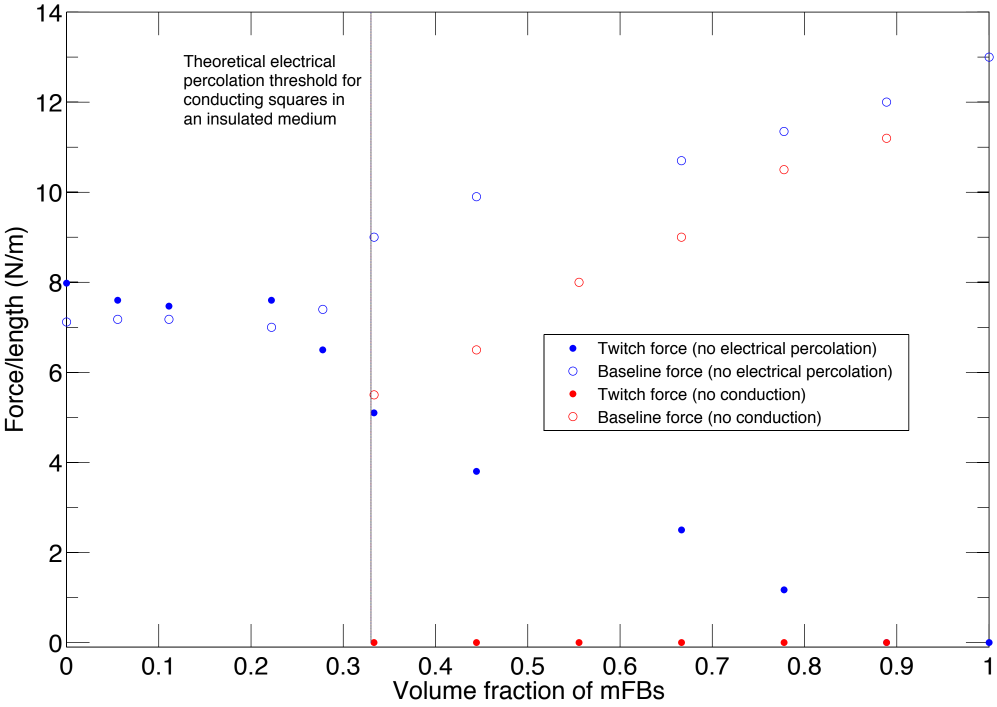

Figure 5.9: Combined mechanical and electrical two-dimensional simulation
The combined mechanical and electrical effects were studied as a function of mFB volume fraction with a two-dimensional electromechanical coupled simulation. Blue points show data assuming no electrical percolation occurred(subsection of cells taken before the conduction block) to understand primarily mechanical effects of mFBs. The red points assumed electrical percolation did occur and subsections of cells were taken from after the conduction block to observe the combined mechanical and electrical effects of mFBs. In this case, after electrical percolation occurs, the CMs no longer depolarize and therefore do not contract. The two data sets are the same until the electrical percolation threshold.

Chapter 6

Future work

Initial experimental results indicated, in moderate concentrations, mFBs improved contractile EHT functioning, but at higher concentrations could impair function. In Chapter 2, this was first studied through a one-dimensional simplified mechanical model of a string of mFBs and CMs in varying ratios. The model supported the experimental results and yielded insight into possible mechanical causes for deleterious effects of mFBs on EHT. In addition to the mechanical effects though, myofibroblasts can impair EHT contractile function by distorting excitatory conduction, and this was the focus of Chapter 3. Electrophysiologic bounds and estimates for conduction velocity in simulations of idealized fibrotic myocardium showed decreased conduction velocity with increased mFB volume fraction, and ultimately failed conduction at a critical mFB volume fraction. Expanding on these simulations in Chapter 4, experimental techniques for estimation of conduction velocity using calcium imaging compared to estimates of measured mFB volume fraction in EHT yielded further insight into the electrical effects of mFBs on EHT. Preliminary results support electrophysiologic simulations with conduction velocity decreasing with increased mFB volume fraction. Finally, Chapter 5 addresses the trade-off between electrical and mechanical percolation effects in two-dimensions. Results show that, in moderate concentrations, mFBs have little effect on overall tissue function, but at a critical mFB volume fraction, twitch force begins to decrease, and then at a critical electrical percolation threshold, conduction is completely blocked and EHT no longer contracts. These results developed a foundation from which a large number of important studies can be launched.

6.1 Optical mapping of entire specimens

Because of limitations on equipment including light and camera speed, optical mapping of the entire specimen was not feasible in this dissertation research. A future goal is to preform optical mapping on entire tissue constructs. Previous attempts have been unsuccessful in sensing any change in fluorescence. Because the speed impulse propagation is very fast (about 5 cm/second), a camera speed of around 500 frames/second is needed to capture the conduction in a 1 cm long tissue. At frame rates this high, the exposure time is very small, and thus, getting enough light is a significant obstacle. Also, while optical mapping has been well established in whole heart samples [6] and in two-dimensional culture [9, 22], the cell density in EHT is much lower, and thus, the accumulative light is lower. Using high numerical aperture lenses with high optical density filters will accumulate maximum light and prevent excitation light from overpowering the fluorescence signal of interest. Also, using a higher quantum efficiency sensor will capture the more light. These techniques should make it possible to observe optical mapping of entire EHT specimens.

6.2 Optical mapping simultaneously with mechanics testing

Another future goal is to capture optical mapping data simultaneously with mechanical force data. The ability to directly compare impulse propagation modulation with mechanical force modulation by mFBs would be a beneficial tool. This direct comparison could be used to study electromechanical coupling in EHT. It would also be essential in delineating the electromechanical cause for fibrotic tissue shutdown. It could indicate conditions in which electrical conduction failure causes fibrotic tissue to cease beating versus conditions in which mechanical or material effects cause failure. Currently methods exist to observe calcium transients in EHT, and extending that to optical mapping was discussed previously. Tools also exist to measure mechanical forces using a force transducer while controlling tissue strain with a stepper motor. Combining these two techniques would be a major step toward better understanding the modulation of EHT by mFBs in a natural three-dimensional environment while retaining the ability control many experimental conditions.

6.3 Infarction scar model

In addition to randomly distributed mFBs within an EHT, future studies will observe the effects of a defined region of mFBs, replicating an infarct scar, on mechanical and electrical function. Mechanical force testing, as described in Chapter 5, and optical imaging, as described in Chapter 4, can be combined to better understand how these models for infarct scars effect overall EHT functioning. EHT with defined regions of mFB have been prepared previously(Fig. 6.1), and studying these through optical mapping and mechanical force testing simultaneously would yield further insight into the interactions of mFBs and CMs.

6.4 Material property analysis

Material parameters used for overall tissue mechanics model were from previously published data. Experimental data exists from mechanical force testing presented Chapter 5 to preform viscoelastic fitting and obtain material parameters for EHT studied here. These results would allow for more accurate parameters and comparison of computational results to experimental results of the exact systems. In addition, to extend beyond the linear study, a nonlinear viscoelastic model fitting and analysis should be done with the experimental EHT force data obtained for these studies.

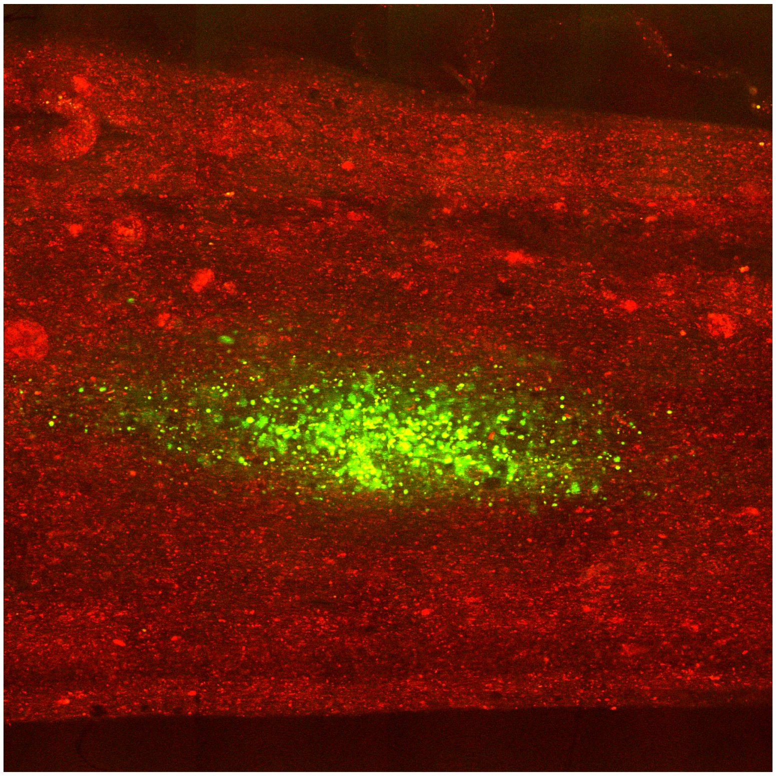

Figure 6.1: EHT with defined region of mFBs
EHT with defined region of mFBs could be used as an experimental model for an infarction scar. In image, Cell Tracker Green is used to label the infarct scar while Cell Tracker Red is used to label the remaining EHT.

6.5 Computational

6.5.1 Nonlinear

The next step computationally is to incorporate non-linearity into the overall tissue viscoelastic mechanics model. Previous studies showed that cells of many types exhibit nonlinear elasticity [40, 34], but as a first step a linear model was used. Using the mechanical testing data obtained in these studies, nonlinear model fitting will yield material properties for such a model. Some anomalies in experimental data indicated the importance of increasing the accuracy of the model to include nonlinearity in future computational studies.

6.5.2 Alternans

Alternans, alternating amplitude of the heart from beat to beat [28], are another important concentration of future studies. Preliminary studies showed that the electrophysiologic model, discussed in Chapter 3, exhibited alternans under certain conditions. Further exploration of this could lead to a sample set of experimental conditions to induce and study alternans in a controlled environment. Limitations to this study are computational power and time. The studies must be run for numerous heart beats to capture the alternans. Better utilizing parallel computing and high power computing capabilities are important for this work. Preliminary single cell calcium imaging at low temporal resolution using Fluo-2 in EHT showed promising possibility of measuring alternans in the experimental setup as well(Fig. 6.2).

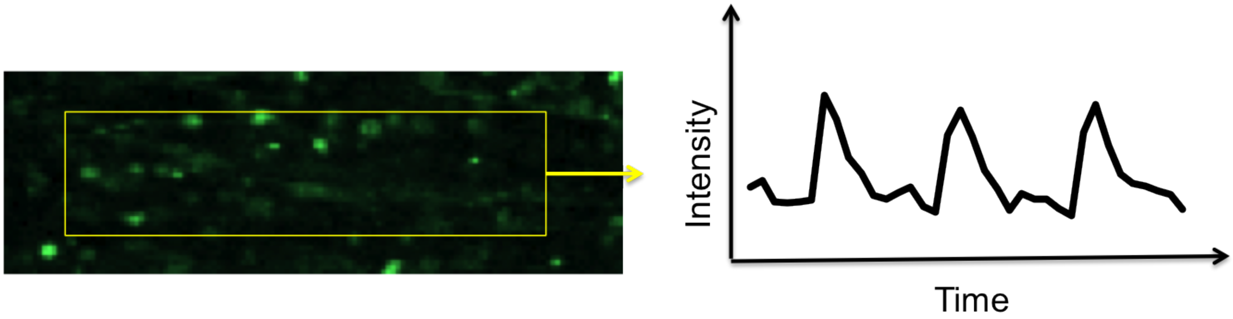

Figure 6.2: Single cell calcium transient
A single cell, labeled with Fluo-2, was imaged with a Zeiss confocal microscope with temporal resolution of approximately 25 ms per frame. Resulting calcium transients indicated the possibility of alternans that could be the subject of future studies in EHT.

6.6 Improving volume fraction estimates

While the current method, described in Chapter 4 and 5, for estimating volume fraction gives a first order approximation of these values, there are many possible improvements to obtain these data more accurately. We are interested in only a few percent of mFBs of total volume, and so getting accurate results for volume fraction is challenging.

Developing a more exact method of calibrating images, so brightness remains the same from data set to data set is one possible improvement. This could be done using fluorescent beads for calibrating the images. This could also be used to calibrate the threshold used for converting the acquired images into binary images for area fraction calculations during image analysis.

Another problem encountered was antibody penetration of the extracellular matrix (ECM) for selectively staining titin. Because we were looking at highly remodeled experimental models for fibrotic myocardium, the dense ECM prevented the antibodies from penetrating and cell staining in certain cases. This could be solved by studying thin tissue slices instead. This would allow the primary and secondary titin antibodies to diffuse into the cells more easily.

Appendix A

Beneficial and deleterious mechanical interactions between myofibroblasts and cardiomyocytes in a one dimensional model supplemental information

A.1 Supplemental Information

A.1.1 Excitation-Contraction Model

To relate approximate calcium transient to contractile force, the model of Hunter et al. [12] is implemented to predict CM contractile stress $T([Ca^{2+}]_i, \lambda, t)$ as a function of time t, the concentration $[Ca^{2+}]_i$ of free myoplasmic Ca^{2+}, and the cellular stretch rate λ and its time history. The internal workings of the model involve four state variables: the concentration$[Ca^{2+}]_b$ of Ca^{2+} bound to troponin C, the fraction z of actin binding sites that are occupied by actomyosin crossbridges, the state-dependent maximum activation stress T_o, and the current contractile stress T. The internal workings begin with a binding kinetics equation for $[Ca^{2+}]_b$, which depends on the current contractile stress T:

$$\frac{d[Ca^{2+}]_b}{dt} = \rho_o[Ca^{2+}]_i([Ca^{2+}]_{b,max} - [Ca^{2+}]_b) - \rho_1(1 - \frac{T}{\gamma T_0})[Ca^{2+}]_b \tag{A.1}$$

where rate constants $\rho_o = 100s^{-1}\mu M^{-1}$ and $\rho_1 = 160s^{-1}$, $\gamma = 2.6$, and $[Ca2+]_{bmax} = 2.26\mu m$ are reasonable values (Hunter, 1998),. $[Ca2+]_b$ determines the rate of change of z:

$$\frac{dz}{dt} = \alpha_o\left((\frac{[Ca^{2+}]_b}{C_{50}})^n(1 - z) - z \right) \tag{A.2}$$

where α_o is a constant and n and $log_{10}(C_{50})$ increase linearly with the degree of stretch γ (Hunter, 1998). The maximum activation stress scales with stretch and with increasing numbers of cross-bridges:

$$T_o = T_{ref}\left(1 + \beta_o(\lambda - 1) \right)z \tag{A.3}$$

where T_{ref}=125 kPa and $\beta_o = 1.45$ for rat trabeculae (Nickerson, 2001). Finally, the Bergel-Hunter fading memory model (Hunter, 1995) is applied to account for the observation that following a step shortening, the cells recover lost tension actively over three distinct timescales:

$$T = T_o\frac{1 + aQ}{1 - Q}, Q = \sum_{i=1}^{3} A_i \int_{-\infty}^{t} exp(-\alpha_i(t - \tau)\frac{d\lambda}{dt}(\tau))d\tau \tag{A.4}$$

where, constants a, A_i, and α_i have been fit by Hunter et al. (Hunter, 1998) for rat trabeculae. Note that Q is most important following rapid length changes. The approximation for intracellular calcium, $[Ca^{2+}]_i$, used Equation 6 from Hunter et. al. 1998, developed from experimental data.

$$Ca_i(t) = Ca_0 + (Ca_{max} - Ca_0)\frac{t}{\tau_{Ca}}e^{1-\frac{t}{\tau_{Ca}}} \tag{A.5}$$

$Ca_i(t)$ here is the time-dependent intracellular concentration of Ca^{2+}, which has a resting level Ca_0 and achieves its maximum value Ca_{max} at time t $=\tau_{Ca}$ with Ca_0=0.01 mM, Ca_{max}=1 mM and τ_{Ca}=60 ms.

A.1.2 Full Finite Element Equations

Equation is in the form:

$$\mathbf{f} = [K]\mathbf{u} + constants \tag{A.6}$$

where f and u are column vectors and K is the global stiffness matrix equal to

$$\begin{bmatrix} 1 & 2 & 3 & ... & i-2 & i-1 & i & i+1 & i+2 & ... & I-2 & I-1 & I \\ k_1^p + \frac{c_1^p}{\Delta t} & -\frac{c_1^p}{\Delta t} & -k_1^p & & & & & & & & & & \\ & & & & & -\frac{c_e^p}{\Delta t} & k_e^s + \frac{c_e^p}{\Delta t} & -k_e^s & & & & & \\ & & & & -k_e^p & -k_e^s & \frac{c_{e+1}^p}{\Delta t} + k_{e+1}^p + k_e^s + k_e^p & -\frac{c_{e+1}^p}{\Delta t} & -k_{e+1}^p & & & & \\ & & & & & & & & & & -k_E^p & -k_E^s & k_E^s + k_E^p \end{bmatrix}$$

Then f equals

$$\begin{bmatrix} f_1 \\ f_{i(even)} \\ f_{i(odd)} \\ f_I \end{bmatrix}$$

and u equals

$$\begin{bmatrix} u_1 \\ u_2 \\ ... \\ u_I \end{bmatrix}$$

and constants equals

$$\begin{bmatrix} \frac{c_1^p}{\Delta t}(-u_1^{j-1} + u_2^{j-1}) + \bar{F}_1^j \\ -\frac{c_e^p}{\Delta t}(-u_{i-1}^{j-1} + u_i^{j-1}) - \bar{F}_e^j \\ \frac{c_{e+1}^p}{\Delta t}(-u_i^{j-1} + u_{i+1}^{j-1}) + \bar{F}_{e+1}^j \\ 0 \end{bmatrix}$$

Appendix B

Summary of model parameters

B.1 Electrophysiologic model

B.1.1 Tissue model

Parameters unless otherwise stated:

mFB membrane capacitance C_f=25 pF
CM membrane capacitance C_f=125 pF
mFB resting potential E_f=-20mV
mFB membrane conductance G_f=4 nS
Gap junction conductances G^{ik}
End to end CM to CM=600 nS Side to side CM=200-1000 nS proportionallu to overlap between cells
CM to mFB=20 nS
mFB to mFB=20 nS

B.1.2 Cell models

Luo-Rudy

Default parameters from published model used [16]: stimulus=80mV CM resting potential E_f=-84 mV Basic cycle length=0.4 seconds

Frequency=1 Hz
Initial potassium concentration k_o=5.4 mM
Initial sodium concentration na_o=140 mM
Initial calcium concentration ca_o=1.8 mM

Luo-Rudy dynamic

Default parameters from published model used [15]:

Inputs stimulus=125 mV CM resting potential E_f=-89 mV Basic cycle length=0.4 seconds
Frequency=1 Hz
Initial potassium concentration k_o=4.5 mM
Initial sodium concentration na_o=140 mM
Initial calcium concentration ca_o=1.8 mM

B.1.3 Excitation-contraction model

Parameters fit to rat ventricular cardiac muscle [12]:

TnC-Ca Binding:

$\rho_0 = 100s^{-1}\mu M^{-1}$, $\rho_1 = 160s^{-1}$, $\gamma = 2.6$, $[Ca^{2+}]_{bmax}$=2.26 μM

Thin filament kinetics:

T_{ref}=100 kPa, n_{ref}=6.9, pC_{50ref}=6.2, α_0=$2s^{-1}$, $\beta_0 = 1.45$, $\beta_1 = 1.95$, $\beta_2 = 0.31$

Crossbridge kinetics:

a=0.5, A_1=50, α_1=$33s^{-1}$, $A_2 = A_3$=175, $\alpha_2 = \alpha_3$=$2850s^{-1}$

Throughout these studies we used $\lambda = 1$ for the ratio of extension of muscle.

B.2 Two-dimensional tissue mechanics model

Model parameters were used from two previously published papers [3, 40] using cross-sectional area estimated from specimens.

Cross-sectional area= 0.2 mm^2

B.2.1 ECM

k^p=20 kPa, k^s=85 kPa, μ=5 kPa s^-1

B.2.2 CMs

k^p=90 kPa, k^s=340 kPa, μ=110 kPa s^-1, $F(t)$=stress input from excitation-contraction model (max twitch force=15kPa, baseline=2kPa)

B.2.3 mFBs

k^p=90 kPa, k^s=585 kPa, μ=245 kPa s^-1, F=10 kPa

References

[1] KW Altman and R. Plonsey. Development of a model for point source electrical fibre bundle stimulation. *Medical and Biological Engineering and Computing*, 26(5):466–475, 1988.

[2] K. Andrew MacCannell, H. Bazzazi, L. Chilton, Y. Shibukawa, R.B. Clark, and W.R. Giles. A mathematical model of electrotonic interactions between ventricular myocytes and fibroblasts. *Biophysical journal*, 92(11):4121–4132, 2007.

[3] C.F. Asnes, J.P. Marquez, E.L. Elson, and T. Wakatsuki. Reconstitution of the frank-starling mechanism in engineered heart tissues. *Biophysical journal*, 91(5):1800–1810, 2006.

[4] D.R. Baker, G. Paul, S. Sreenivasan, and H.E. Stanley. Continuum percolation threshold for interpenetrating squares and cubes. *Physical Review E*, 66(4):046136, 2002.

[5] ALR Bug, SA Safran, G.S. Grest, and I. Webman. Do interactions raise or lower a percolation threshold? *Physical review letters*, 55(18):1896–1899, 1985.

[6] I.R. Efimov, V.P. Nikolski, and G. Salama. Optical imaging of the heart. *Circulation research*, 95(1):21–33, 2004.

[7] T. Eschenhagen, C. Fink, U. Remmers, H. Scholz, J. Wattchow, J. Weil, W. Zimmermann, HH Dohmen, H. Schafer, N. Bishopric, et al. Three-dimensional reconstitution of embryonic cardiomyocytes in a collagen matrix: a new heart muscle model system. *The FASEB journal*, 11(8):683, 1997.

[8] G.M. Faber, J. Silva, L. Livshitz, and Y. Rudy. Kinetic properties of the cardiac l-type ca2+ channel and its role in myocyte electrophysiology: a theoretical investigation. *Biophysical journal*, 92(5):1522–1543, 2007.

[9] G. Gaudesius, M. Miragoli, S.P. Thomas, and S. Rohr. Coupling of cardiac electrical activity over extended distances by fibroblasts of cardiac origin. *Circulation research*, 93(5):421–428, 2003.

[10] Z. Hashin and S. Shtrikman. Conductivity of polycrystals. *Physical Review*, 130(1):129, 1963.

[11] P.J. Hunter. Myocardial constitutive laws for continuum mechanics models of the heart. *Advances in experimental medicine and biology*, 382:303, 1995.

[12] PJ Hunter, AD McCulloch, and H. Ter Keurs. Modelling the mechanical properties of cardiac muscle. *Progress in biophysics and molecular biology*, 69(2-3):289–331, 1998.

[13] D.A. Kass, J.G.F. Bronzwaer, and W.J. Paulus. What mechanisms underlie diastolic dysfunction in heart failure? *Circulation research*, 94(12):1533–1542, 2004.

[14] P. Kohl. Heterogeneous cell coupling in the heart an electrophysiological role for fibroblasts. *Circulation research*, 93(5):381–383, 2003.

[15] L.M. Livshitz and Y. Rudy. Regulation of ca2+ and electrical alternans in cardiac myocytes: role of camkii and repolarizing currents. *American Journal of Physiology-Heart and Circulatory Physiology*, 292(6):H2854–H2866, 2007.

[16] C. Luo and Y. Rudy. A model of the ventricular cardiac action potential. depolarization, repolarization, and their interaction. *Circulation research*, 68(6):1501–1526, 1991.

[17] I. Manabe, T. Shindo, and R. Nagai. Gene expression in fibroblasts and fibrosis. *Circulation research*, 91(12):1103–1113, 2002.

[18] J.P. Marquez, E.L. Elson, and G.M. Genin. Whole cell mechanics of contractile fibroblasts: relations between effective cellular and extracellular matrix moduli. *Philosophical Transactions of the Royal Society A: Mathematical, Physical and Engineering Sciences*, 368(1912):635, 2010.

[19] J.P. Marquez, G.M. Genin, K.M. Pryse, and E.L. Elson. Cellular and matrix contributions to tissue construct stiffness increase with cellular concentration. *Annals of biomedical engineering*, 34(9):1475–1482, 2006.

[20] J.P. Marquez, G.M. Genin, G.I. Zahalak, and E.L. Elson. The relationship between cell and tissue strain in three-dimensional bio-artificial tissues. *Biophysical journal*, 88(2):778–789, 2005.

[21] J.P. Marquez, G.M. Genin, G.I. Zahalak, and E.L. Elson. Thin bio-artificial tissues in plane stress: the relationship between cell and tissue strain, and an improved constitutive model. *Biophysical journal*, 88(2):765–777, 2005.

[22] M. Miragoli, G. Gaudesius, and S. Rohr. Electrotonic modulation of cardiac impulse conduction by myofibroblasts. *Circulation research*, 98(6):801–810, 2006.

[23] A. Nekouzadeh, K.M. Pryse, E.L. Elson, and G.M. Genin. Stretch-activated force shedding, force recovery, and cytoskeletal remodeling in contractile fibroblasts. *Journal of biomechanics*, 41(14):2964–2971, 2008.

[24] DP Nickerson, NP Smith, and PJ Hunter. A model of cardiac cellular electromechanics. *Philosophical Transactions of the Royal Society of London. Series A: Mathematical, Physical and Engineering Sciences*, 359(1783):1159, 2001.

[25] W. Prager. On the formulation of constitutive equations for living soft tissues(constitutive equations for living soft tissues freely deforming under negligible stresses with hooke law as limit). *Quarterly of Applied Mathematics*, 27:128–132, 1969.

[26] Z. Qu, Y. Shiferaw, and J.N. Weiss. Nonlinear dynamics of cardiac excitation-contraction coupling: an iterated map study. *Physical Review E*, 75(1):011927, 2007.

[27] S. Rohr. Myofibroblasts in diseased hearts: new players in cardiac arrhythmias? *Heart Rhythm*, 6(6):848–856, 2009.

[28] D.S. Rosenbaum, L.E. Jackson, J.M. Smith, H. Garan, J.N. Ruskin, and R.J. Cohen. Electrical alternans and vulnerability to ventricular arrhythmias. *New England Journal of Medicine*, 330(4):235–241, 1994.

[29] M.S. Spach, J.F. Heidlage, P.C. Dolber, and R.C. Barr. Mechanism of origin of conduction disturbances in aging human atrial bundles: experimental and model study. *Heart Rhythm*, 4(2):175–185, 2007.

[30] S.A. Thompson, C.R. Copeland, D.H. Reich, and L. Tung. Mechanical coupling between myofibroblasts and cardiomyocytes slows electric conduction in fibrotic cell monolayersclinical perspective. *Circulation*, 123(19):2083–2093, 2011.

[31] S. Torquato and HW Haslach Jr. Random heterogeneous materials: microstructure and macroscopic properties. *Applied Mechanics Reviews*, 55:B62, 2002.

[32] N.A. Trayanova and J.J. Rice. Cardiac electromechanical models: from cell to organ. *Frontiers in Physiology*, 2, 2011.

[33] E. Vigmond, F. Vadakkumpadan, V. Gurev, H. Arevalo, M. Deo, G. Plank, and N. Trayanova. Towards predictive modelling of the electrophysiology of the heart. *Experimental physiology*, 94(5):563–577, 2009.

[34] T. Wakatsuki, M.S. Kolodney, G.I. Zahalak, and E.L. Elson. Cell mechanics studied by a reconstituted model tissue. *Biophysical journal*, 79(5):2353–2368, 2000.

[35] T. Wakatsuki, B. Schwab, N.C. Thompson, and E.L. Elson. Effects of cytochalasin d and latrunculin b on mechanical properties of cells. *Journal of cell science*, 114(5):1025, 2001.

[36] WO Williams. Huxleys model of muscle contraction with compliance. *Journal of Elasticity*, pages 1–16, 2011.

[37] L.H. Xie, D. Sato, A. Garfinkel, Z. Qu, and J.N. Weiss. Intracellular ca alternans: coordinated regulation by sarcoplasmic reticulum release, uptake, and leak. *Biophysical journal*, 95(6):3100–3110, 2008.

[38] Y. Xie, A. Garfinkel, P. Camelliti, P. Kohl, J.N. Weiss, and Z. Qu. Effects of fibroblast-myocyte coupling on cardiac conduction and vulnerability to reentry: a computational study. *Heart Rhythm*, 6(11):1641–1649, 2009.

[39] Y. Xie, A. Garfinkel, J.N. Weiss, and Z. Qu. Cardiac alternans induced by fibroblast-myocyte coupling: mechanistic insights from computational models. *American Journal of Physiology-Heart and Circulatory Physiology*, 297(2):H775, 2009.

[40] G.I. Zahalak, J.E. Wagenseil, T. Wakatsuki, and E.L. Elson. A cell-based constitutive relation for bio-artificial tissues. *Biophysical Journal*, 79(5):2369–2381, 2000.

[41] R. Zak. Cell proliferation during cardiac growth. *The American journal of cardiology*, 31(2):211, 1973.

[42] W.H. Zimmermann, I. Melnychenko, and T. Eschenhagen. Engineered heart tissue for regeneration of diseased hearts. *Biomaterials*, 25(9):1639–1647, 2004.

Vita

Teresa M. Abney

Date of Birth	May 10, 1985
Place of Birth	Joliet, Illinois
Degrees	Ph.D. Mechanical Engineering,Washington University in St. Louis, May 2012 M.S. Mechanical Engineering, Washington University in St. Louis, December 2010 B.S. Magna Cum Laude, Mechanical Engineering, Southern Illinois University Carbondale, May 2007
Professional Societies	American Society of Mechanical Engineers Society of Women Engineers
Publications	Abney, T.M., Feng, Y., Okamoto, R.J., Pless, R.,Genin, G.M., Bayly, P.V., Principal components of brain displacement during angular acceleration of the human head in vivo. PLoS ONE 6(7): e22063, July 14, 2011. Feng, Y., Abney, T.M., Okamoto, R.J., Pless, R.,Genin, G.M., Bayly, P.V., Relative Brain Displacement and Deformation During Mild Frontal Head Impact, Journal of the Royal Society Interface, 7 (53): 1677-1688. Genin G.M., Abney, T.M., Wakatsuki T., Elson E.L., "Cell-cell interactions and the mechanics of cells and tissues." In Mechanobiology of Cell-Cell & Cell-Matrix Interactions, A. J. Wagoner-Johnson and B. Harley, eds. New York: Springer, 2010.

May 2012

Interactions of Cardiomyocytes and Myofibroblasts, Abney, Ph.D. 2012